Atmos. Chem. Phys. Discuss., https://doi.org/10.5194/acp-2018-126
Manuscript under review for journal Atmos. Chem. Phys.
Discussion started: 20 February 2018

Aerosol as a potential factor to control the increasing torrential rain events in urban areas over the last decades

Seoung Soo Lee[1], Zhanqing Li[1], Yong-Sang Choi[2], and Chang-Hoon Jung[3]

[1]Earth System Science Interdisciplinary Center, University of Maryland, Maryland

[2]Department of Environmental Science and Engineering, Ewha Womans University, Seoul, South Korea

[3]Department of Health Management, Kyungin Women's University, Incheon, South Korea

Corresponding author: Seoung Soo Lee
Office: (303) 497-6615
Cell: (609) 375-6685
Fax: (303) 497-5318
E-mail: cumulss@gmail.com, slee1247@umd.edu

Atmos. Chem. Phys. Discuss., https://doi.org/10.5194/acp-2018-126
Manuscript under review for journal Atmos. Chem. Phys.
Discussion started: 20 February 2018

Abstract

This study examines the role played by aerosol in torrential rain that occurred in Seoul, which is a metropolitan area where urbanization has been rapid in the last few decades, using cloud-system resolving model (CSRM) simulations. The model results show that the inhomogeneity of the spatial distribution of aerosol concentrations or loading causes the inhomogeneity of the spatial distribution of evaporative cooling and the intensity of associated outflow around the surface. This inhomogeneity generates a strong convergence field in which torrential rain forms. With the increases in the inhomogeneity of the spatial distribution of aerosol concentrations, the occurrence of torrential rain increases. This study finds that the effects of the increases in the inhomogeneity play a much more important role in the increases in torrential rain than the much-studied effects of the increases in aerosol loading. Results in this study demonstrate that for a better understanding of extreme weather events such as torrential rain in urban areas, not only changing aerosol loading but also changing aerosol spatial distribution since industrialization should be considered in aerosol-precipitation interactions.

Atmos. Chem. Phys. Discuss., https://doi.org/10.5194/acp-2018-126
Manuscript under review for journal Atmos. Chem. Phys.
Discussion started: 20 February 2018

1. Introduction

It has been reported that there has been an increase in the frequency or occurrence of torrential rain in urban areas over the last decades (Bouvette et al., 1982; Diem and Brown, 2003; Fujibe, 2003; Takahashi, 2003; Burian and Shepherd, 2005; Shepherd, 2005; Chen et al., 2015). Over the last decades, population in urban areas has increased significantly. In 1950, 30 % of the whole population in the world lived in urban areas, however, in 2010, 54 % of the whole population lived in urban areas. It is predicted that in 2050, 66 % of the whole population will live in urban areas (United Nations, 2015). In addition, urban areas are the centers of economic activity and play a key role in economic productivity (United Nations, 2015). Hence, the increase in the frequency of torrential rain, which has substantial negative impacts on human life and properties by causing events such as flooding and landslide, particularly in urban areas has important social and economic implications.

The torrential rain in urban areas frequently involves the highly inhomogeneous spatial distributions of precipitation (Dhar and Nandergi, 1993; Mannan et al., 2013). While some districts in a city experience light precipitation, other districts in the city experience extremely heavy precipitation or torrential rain for an identical mesoscale convective system (MCS) that covers the whole city area (e.g., Sauer et al., 1984; Korea Meteorological Administration, 2011). Note that this type of the MCS is forced by synoptic- or large-scale temperature and humidity forcings. These "synoptic-scale" forcings tend to be spatially homogeneous in the MCS whose spatial scale is at mesoscale and thus much smaller than that of the forcings. Hence, these forcings tend to intensify all of cloud cells in the MCS in an approximately homogeneous fashion, which tend to produce cloud cells with a similar intensity. These cloud cells with the similar intensity are likely to result in the homogeneous distribution of precipitation over a domain of interest, since cloud cells with the similar intensity are likely to produce the similar precipitation. This indicates that the consideration of the synoptic-scale forcings alone is not able to explain the occurrence of torrential rain which is associated with the inhomogeneous spatial distribution of precipitation. Note that numerous numerical weather prediction studies have utilized the concept of the synoptic-scale forcings to identify mechanisms that control the inhomogeneity of precipitation distributions and associated torrential rain. This is one of the reasons these studies have shown low forecast accuracy for torrential rain and not been able to provide a clear picture of the mechanisms (Mladek et al., 2000; Yeh and Chen, 2004; Mannan et al., 2013). The highly inhomogeneous distribution of precipitation means that there are highly inhomogeneous variables which disrupt the synoptic-forcing-induced homogeneity of the MCS in urban or metropolitan areas. Aerosol is one of the most representative variables that have the high-degree spatial inhomogeneity. In particular, urban aerosol particles are produced by randomly distributed or moving sources (e.g., traffic), which enables aerosol to have the high-degree inhomogeneity in urban areas.

It is well-known that increasing aerosol loading alters cloud microphysical properties such as cloud-particle size and autoconversion. Droplets or cloud-liquid particles collide and collect each other to grow to be raindrops and this growth process is referred to as autoconversion. These collision and collection are more efficient when particle sizes are larger. Hence, increasing aerosol loading, which is known to reduce the particle size, reduces the efficiency of the growth of cloud-liquid particles to raindrops via autoconversion. This results in more cloud liquid which is not grown or converted to raindrops and thus in more cloud liquid mass as a source of evaporation and freezing. It has been shown that aerosol-induced increases in cloud-liquid mass and associated increases in freezing of cloud liquid can enhance parcel buoyancy and thus invigorate convection (Li et al., 2011; Wang et al., 2014). The invigorated convection can enhance precipitation. The aerosol-induced increases in cloud-liquid mass and associated increases in evaporation can intensify gust fronts, which in turn intensify the subsequently developing convective clouds and enhance the precipitation (Khain et al., 2005; Seifert and Beheng, 2006; Tao et al., 2007; van den Heever and Cotton, 2007; Storer et al., 2010; Tao et al., 2012; Lee and Feingold, 2013; Lee et al., 2017). These aerosol-induced invigoration and intensification of convection or convective clouds raise the possibility that the high-degree inhomogeneity of aerosol in tandem with the increasing aerosol loading can generate and enhance torrential rain which can involve the inhomogeneity of precipitation and associated cloud intensity in urban areas. For example, cloud cells (in a MCS) sitting on a district with a higher aerosol concentration in a city can be invigorated more than those cells on other districts with a lower aerosol concentration in the city. This can lead to enhanced precipitation and possibly torrential rain at the district, while in other districts, there can be less precipitation. This creates the inhomogeneity of precipitation distributions that can accompany torrential rain in a specific area. The further increase in aerosol loading at the district with the higher aerosol concentration will further enhance precipitation and torrential rain there and thus create the greater inhomogeneity of precipitation distributions. Motivated by this, numerical simulations are performed by using a cloud-system resolving model (CSRM) that resolves cloud-scale microphysical and dynamic processes and simulates the effect of the inhomogeneity and loading of aerosol on precipitation.

Using the CSRM, an observed MCS that involves deep convective clouds and torrential rain is simulated. Here, deep convective clouds reach the tropopause. For the simulations, we select the MCS over the Seoul area (in Korea) that has a population of ~ten millions and thus is one of the representative metropolitan areas around the world. These simulations are to identify key mechanisms that are associated with cloud-scale microphysics and dynamics and explain the generation of the inhomogeneity of precipitation and associated torrential rain in terms of the spatial inhomogeneity and loading of aerosol.

2. CSRM

As a CSRM, we use the Advanced Research Weather Research and Forecasting (ARW) model (version 3.3.1), which is a nonhydrostatic compressible model. Prognostic microphysical variables are transported with a 5th-order monotonic advection scheme (Wang et al., 2009). Shortwave and longwave radiation parameterizations have been included in all simulations by adopting the Rapid Radiation Transfer Model (RRTMG; Mlawer et al., 1997; Fouquart and Bonnel, 1980).

To represent the microphysical processes, the CSRM adopts the bin scheme. The bin scheme adopted by the CSRM is based on the Hebrew University Cloud Model (HUCM) described by Khain et al. (2009). The bin scheme solves a system of kinetic equations for the size distribution functions for water drops, ice crystals (plate, columnar and branch

Atmos. Chem. Phys. Discuss., https://doi.org/10.5194/acp-2018-126
Manuscript under review for journal Atmos. Chem. Phys.
Discussion started: 20 February 2018

types), snow aggregates, graupel and hail, as well as cloud condensation nuclei (CCN). Each size distribution is represented by 33 mass doubling bins, i.e., the mass of a particle m_k in the k bin is determined as $m_k = 2m_{k-1}$.

3. Case description and simulations

3.1 Control run

A three-dimensional simulation of the observed MCS, i.e., the control run, is performed over a one-day period. The control run consists of two-way interactive triple-nested domains with a Lambert conformal map projection (Figure 1). A domain with a 500-m resolution covering the Seoul area (Domain 3) is nested in a domain with a 1.5-km resolution (Domain 2), which in turn is nested in a domain with a 4.5-km resolution (Domain 1). All domains have 84 vertical layers with a terrain following sigma coordinate, and the model top is 50 hPa. Note that the cumulus parameterization scheme is used in Domain 1 but not used in Domain 2 and Domain 3 where convective rainfall generation is assumed to be explicitly resolved.

The MCS was observed over Seoul, Korea (09:00 LST (local solar time) July 27th – 09:00 LST July 28th 2011). A significant amount of precipitation is recorded during this period, with a local maximum value of ~ 200.0 mm hr^{-1}. This heavy rainfall caused flash floods and landslides on a mountain at the southern flank of the city, leading to the deaths of 60 people (Korea Meteorological Administration, 2011). At 21:00 LST July 26th 2011, favorable synoptic-scale features for the development of the selected MCS and heavy rainfall were observed. The western Pacific subtropical high (WPSH) was located over the southeast of Korea and Japan, and there was a low-pressure trough over north China (Figure 2). Low-level jets between the flank of the WPSH and the low-pressure system brought warm, moist air from the Yellow Sea to the Korean Peninsula (Figure 2). Transport of warm and moist air by the southwesterly low-level jet is an important condition for the development of heavy rainfall events over the Korean Peninsula (Hwang and Lee 1993; Lee et al. 1998; Sun and Lee 2002).

Reanalysis data, which are produced by the Met Office Unified Model (Brown et al., 2012) and recorded continuously every 6 hours on a 0.11° × 0.11° grid, provide the initial and boundary conditions of potential temperature, specific humidity, and wind for the simulation. These data represent large- or synoptic-scale environment. For the simulation, we adopt an open lateral boundary condition. Using the Noah land surface model (LSM; Chen and Dudhia, 2001), surface heat fluxes are predicted.

The current version of the ARW model assumes the homogeneity of aerosol properties or a constant background aerosol concentration over the simulation domain and period. For the control run that focuses on the effect of aerosol on torrential rain in an urban area (i.e., Seoul area or Domain 3) where aerosol properties such as composition and number concentration vary significantly in terms of time and space, we abandon this assumption of the homogeneity and consider the spatiotemporal inhomogeneity of aerosol properties over the urban area. For this, we develop an aerosol module that is able to accept the inhomogeneity of aerosol properties and apply it to cloud microphysical and radiative processes. This developed aerosol module is now implemented to the ARW model.

The inhomogeneity of aerosol properties is observed by surface sites that measure aerosol mass (PM_{10}) in Seoul. These sites are distributed with ~1-km distance between them and measure aerosol mass every ~10 minutes, which enables us to resolve the inhomogeneity with high spatiotemporal resolutions. However, the measurement of other aerosol properties such as aerosol composition and size distributions in those sites is absent. There are several additional sites of the aerosol robotic network (AERONET; Holben et al., 2001) in the Seoul area. Distances between these AERONET sites are ~10 km, hence, they do not provide data whose resolutions are as high as those of the PM_{10} data. However, the AERONET sites provide information on aerosol composition and size distributions. While using data from the high-resolution PM_{10} sites to represent the inhomogeneity of aerosol properties over the Seoul area, we use the relatively low-resolution data from the AERONET sites to represent aerosol composition and size distributions.

The AERONET measurements indicate that overall, aerosol particles in Seoul during the MCS period follow the tri-modal log-normal distribution and aerosol particles, on average, are an internal mixture of 60 % ammonium sulfate and 40 % organic compound. The organic compound is assumed to be water soluble and composed of (by mass) 18 % levoglucosan ($C_6H_{10}O_5$, density = 1600 kg m^{-3}, van't Hoff factor = 1), 41 % succinic acid ($C_6O_4H_6$, density = 1572 kg m^{-3}, van't Hoff factor = 3), and 41 % fulvic acid ($C_{33}H_{32}O_{19}$, density = 1500 kg m^{-3}, van't Hoff factor = 5) based on a simplification of observed chemical composition. Based on this, in this study, the tri-modal log-normal distribution is assumed for the size distribution of background aerosol as shown in Figure 3 and the internal mixture is adopted by aerosol particles. The assumed size distribution of background aerosol is obtained by averaging size distribution parameters (i.e., modal radius and standard deviation of each of nuclei, accumulation and coarse modes, and the partition of aerosol number among those modes) over the AERONET sites and the MCS period. With these assumption and adoption, PM_{10} is converted to background aerosol number concentrations. Figures 4a and 4b show the example spatial distributions of background aerosol number concentrations at the surface, which are applied to the control run and represented by black contours. These distributions in Figures 4a and 4b are calculated based on the surface observation in Domain 3 (which covers the Seoul area) at 19:00 and 20:00 LST July 27th 2011, respectively.

Blue contours or lines in Figures 4a and 4b surround areas with the observed heavy precipitation or torrential rain on which this study focuses. In this study, when the precipitation rate at the surface is 60 mm hr^{-1} or above, related precipitation is considered heavy precipitation or torrential rain. There is no one universal designated rate (of precipitation) above which precipitation is considered heavy precipitation and the designated rate varies among countries. 60 mm hr^{-1} as a precipitation rate is around the upper end of the variation. Those blue contours are further discussed below in Results. The red contours or lines in Figures 4a and 4b are defined and discussed below in Results.

In clouds, the aerosol size distribution evolves with sinks and sources, which include advection, droplet nucleation, and aerosol regeneration from droplet evaporation (Fan et al., 2009). Aerosol activation is calculated according to the Köhler theory, i.e., aerosol particles with radii exceeding the critical value at a grid point are activated to become droplets based on predicted supersaturation, and the corresponding bins of the aerosol spectra are emptied. After activation, the aerosol mass is transported within

Atmos. Chem. Phys. Discuss., https://doi.org/10.5194/acp-2018-126
Manuscript under review for journal Atmos. Chem. Phys.
Discussion started: 20 February 2018

hydrometeors by collision-coalescence and removed from the atmosphere once hydrometeors that contain aerosols reach the surface. Aerosol particles return to the atmosphere upon evaporation or sublimation of hydrometeors that contain them. It is assumed that in the planetary boundary layer (PBL), the background aerosol concentration does not vary but above the PBL, the background aerosol concentration reduces exponentially. It is also assumed that in non-cloudy areas, aerosol size and spatial distributions are set to follow the background counterparts. In other words, once clouds disappear completely at any grid points, aerosol size distribution and number concentration at those points recover to the background counterparts. This assumption has been used by numerous CSRM studies and proven to simulate overall aerosol properties and their impacts on clouds and precipitation reasonably well (Morrison and Grabowski, 2011; Lebo and Morrison, 2014; Lee et al., 2016).

3.2 The other runs

In Figures 4a and 4b, there is a high-degree spatial inhomogeneity of background aerosol concentrations in the Seoul area or Domain 3. This inhomogeneity is generated by the contrast between the high aerosol concentrations in the western part of the domain where aerosol concentration is greater than 1500 cm^{-3}, and the low aerosol concentrations in the eastern part of the domain where aerosol concentration is ~700 cm^{-3} or less.

As mentioned above, this study focuses on the effect of the spatial inhomogeneity and loading (or concentrations) of aerosol on precipitation. To better identify and elucidate the effect, the control run is repeated but with the above-mentioned contrast or inhomogeneity that is reduced. To reduce the contrast, over the whole simulation period, the concentrations of background aerosol in the western part of the domain are reduced by a factor of 2, while those in the eastern part do not change. This means that the reduction in the inhomogeneity accompanies that in aerosol concentrations, which enables us to examine both the effects of the inhomogeneity and those of concentrations. Note that the high and the low aerosol concentrations on the left (or western) side and the right (or eastern) side of the domain, respectively, are maintained throughout the whole simulation period, although the location of the boundary between those sides changes

Atmos. Chem. Phys. Discuss., https://doi.org/10.5194/acp-2018-126
Manuscript under review for journal Atmos. Chem. Phys.
Discussion started: 20 February 2018

with time. Here, in the process of the reduction in the contrast, no changes are made for aerosol chemical composition and size distribution in both parts of the domain. As examples, the spatial distribution of background aerosol concentrations at the surface with the reduced contrast at 19:00 and 20:00 LST July 27th 2011 is shown in Figures 4c and 4d, respectively. With the reduced contrast and concentrations or loading, the inhomogeneity and concentrations of aerosol are lower in this repeated run than in the control run. The repeated simulation has the "low" inhomogeneity and concentrations of "aerosol" as compared to the control run and thus is referred to as the low-aerosol run. Comparisons between the control run and the low-aerosol run give us a chance to better understand the role played by the spatial inhomogeneity and loading of aerosol in the spatial distribution of precipitation which involves torrential rain.

In addition to the control run and the low-aerosol run, there are more simulations that are performed to better understand the effect of aerosol on precipitation here. While a detailed description of those simulations is given in the following sections, a brief description is given in Table 1.

4. Results

In this study, analyses of results are performed only in the Seoul area (or Domain 3) where the 500-m resolution is applied. Hence, in the following, the description of the simulation results and their analyses are all only over Domain 3, unless otherwise stated.

4.1 Microphysics and precipitation

4.1.1 Cumulative precipitation

The area-mean precipitation rate at the surface smoothed over 3 hours for the control run and the low-aerosol run is depicted in Figure 5. The simulated precipitation rate in the control run follows the observed counterpart well, which demonstrates that simulations are performed reasonably well. Here, observed precipitation is obtained from the

Atmos. Chem. Phys. Discuss., https://doi.org/10.5194/acp-2018-126
Manuscript under review for journal Atmos. Chem. Phys.
Discussion started: 20 February 2018

measurement by automatic weather system (AWS) at the surface. AWS has a spatial resolution of ~3km. Also, the temporal evolution of the mean precipitation rate in the control run is very similar to that in the low-aerosol run. Associated with this similarity, the averaged cumulative precipitation over the domain at the last time step for the control run is 154.7 mm, which is just ~3 % greater than 150.2 mm for the low-aerosol run.

4.1.2 Precipitation fields and frequency distributions

Figure 6a shows the frequency distribution of precipitation rates that are collected over all of time steps and all of grid points at the surface in the simulations. In Figure 6a, the frequency distribution of observed precipitation rates that are interpolated to those grid points and time steps in the simulations is also shown. The observed maximum precipitation rate is ~180 mm hr^{-1}, which is similar to that in the control run. Also, the overall distribution of observed frequency is consistent well with the simulated counterpart in the control run, although it appears that particularly for heavy precipitation with rates above 60 mm hr^{-1}, the simulated frequency is underestimated as compared to the observed counterpart. The overall difference in the frequency distribution between observation and the control run is much smaller than that between the control run and the low-aerosol run. Hence, we assume that the difference between observation and the control run is considered negligible as compared to that between the runs. Based on this, when it comes to discussion about the difference between the control run and the low-aerosol run, results in the control run can be assumed to be benchmark results against which the effect of the decrease in the spatial inhomogeneity and concentrations of aerosol on results in the low-aerosol run can be assessed.

While we do not see a large difference in cumulative precipitation between the control run (154.7 mm) and the low-aerosol run (150.2 mm), the frequency distribution of precipitation rates shows distinctively different features between the two runs (Figure 6a). For precipitation with rates above 60 mm hr^{-1} or heavy precipitation, the cumulative frequency is ~60 % higher for the control run. For certain ranges of precipitation rates above 60 mm hr^{-1}, there are increases in the frequency or occurrence by a factor of as much as ~10 to ~100. Moreover, for precipitation rates above 120 mm hr^{-1}, while there is the presence of precipitation in the control run, there is no precipitation in the low-aerosol run. Hence, we see that there are significant increases in the frequency or the occurrence of heavy precipitation or torrential rain in the control run as compared to that in the low-aerosol run.

Figure 7 shows the spatial distributions of precipitation rates at the surface. Figures 7a and 7b show those distributions at 17:00 LST July 27th 2011 corresponding to the initial stage of precipitating system in the control run and the low-aerosol run, respectively. In Figure 7, blue contours represent precipitation rates and the other contours are explained after the discussion of blue contours. At 17:00 LST, there is a small area of precipitation around the northwest corner of the domain in both the control run and the low-aerosol run. This implies that a small cloud system develops around the northwest corner of the domain at 17:00 LST. The size of the system and its precipitation area grow with time and at 19:00 LST, the size is much larger (Figures 7c and 7d). The maximum precipitation rate reaches ~100 mm hr^{-1} when time progresses to 19:00 LST (Figure 6b). Heavy precipitation is concentrated in a specific area (surrounded by the green rectangle) in both of the runs (Figures 7c and 7d). The green rectangle surrounds a specific area where more than 90 % of the whole events of heavy precipitation (over the domain) with rates above 60 mm hr^{-1} occur at a specific time in each of the runs. The location of the specific area in the control run is consistent well with the location of heavy precipitation in observation as seen in comparisons between Figures 4a, 7c, and 8a. Figure 8a shows the blue contour in Figure 4a and the green rectangle in Figure 7c for better observation of the consistency. This demonstrates that the simulation of the spatial distribution of heavy precipitation is performed reasonably well. Between 17:00 LST and 19:00 LST, we do not see significant differences in the frequency distribution of precipitation rates, particularly in heavy precipitation with rates above 60 mm hr^{-1} between the runs (Figure 6b).

With the time progress to 20:00 LST, the maximum precipitation rate or the maximum rate of torrential rain reaches ~130 mm hr^{-1} for the control run and ~110 mm hr^{-1} for the low-aerosol run (Figure 6c). Associated with this, between 19:00 and 20:00 LST, significant differences in the frequency distributions, particularly for heavy precipitation between the runs, start to appear (Figure 6c). At 20:00 LST as seen in

Figure 7e and in the previous hours, in the control run, more than 90 % of the heavy precipitation events are concentrated in a specific area that is surrounded by the green rectangle. Note that only in this specific area, the extremely heavy precipitation with rates above 100 mm hr^{-1} occurs. In the low-aerosol run, the extremely heavy precipitation with rates above 100 mm hr^{-1} also occurs only in a particular area, which is surrounded by the green rectangle, at 20:00 LST (Figure 7f). At 20:00 LST, as seen in Figure 4b, observation shows that there are the five spots of heavy precipitation. The location of the largest spot where most of the heavy precipitation events occur is similar to that of the specific area that is surrounded by the green rectangle in the control run as seen in comparisons between Figures 4b, 7e and 8b. Figure 8b shows the blue contour in Figure 4b and the green rectangle in Figure 7e for better observation of the similarity. This again demonstrates that the simulation of the spatial distribution of heavy precipitation is performed with fairly good confidence.

The system continues to evolve after 20:00 LST in a way that its easternmost part is closer to the east boundary of the domain as seen in comparisons between Figure 7e (Figure 7f) and Figure 7g (Figure 7h) for the control (low-aerosol) run. As seen in Figure 7g and in the previous hours, for the control run, more than 90 % of the heavy precipitation events are concentrated in a specific area (surrounded by the green rectangle) at 23:00 LST. However, in the low-aerosol run, it appears that heavy precipitation is not concentrated in a specific area at 23:00 LST. Unlike the green rectangle in the control run at 23:00 LST, the green rectangle at 23:00 LST in the low-aerosol run surrounds an area where ~50 % of the heavy precipitation events are located, although the rectangle surrounds the largest area with heavy precipitation among the heavy precipitation areas in the low-aerosol run. For a period between 20:00 and 23:00 LST as compared to that between 19:00 and 20:00 LST, the maximum precipitation rate rises up to ~180 mm hr^{-1} in the control run, however, in the low-aerosol run, the maximum precipitation rate stays at ~120 mm hr^{-1} (Figures 6c and 6d). Hence, there is the presence of the precipitation rates between ~120 and ~180 mm hr^{-1} in the control run, while there is their absence in the low-aerosol run for the period between 20:00 and 23:00 LST. This reflects that increases in the frequency of torrential rain, which are induced by increases in the spatial

Atmos. Chem. Phys. Discuss., https://doi.org/10.5194/acp-2018-126
Manuscript under review for journal Atmos. Chem. Phys.
Discussion started: 20 February 2018

inhomogeneity and loading of aerosol, enhance, as the system evolves from its initial stage before 20:00 LST to mature stage between 20:00 and 23:00 LST.

After 23:00 LST July 27th 2011, the precipitating system enters its decaying stage. Figure 6e shows the precipitation-rate frequency for a period between 04:00 and 05:00 LST July 28th 2011. As seen in Figure 6e, with the progress of the decaying stage, the maximum precipitation rate reduces down to ~25 mm hr^{-1} as an indication that heavy precipitation disappears and the system is nearly at its end of the life cycle.

4.2 Dynamics

4.2.1 Convergence

As shown in Lee et al. (2008a and 2008b) and Khain et al. (2008), condensation acts as a main source of precipitation by providing cloud liquid as a source of accretion of cloud liquid by precipitable hydrometeors. Condensation is produced by updrafts that control supersaturation and updrafts are rooted in convergence around the surface. As the basic principle of dynamics indicates, air that converges around the surface induces upward motion (or updrafts) to satisfy mass conservation. The stronger convergence of air induces stronger updrafts and then more condensation. As a first step to the examination of condensation, convergence fields at the surface are obtained and the column-averaged condensation rates are superimposed on them as shown in Figure 7. In Figure 7, the convergence and condensation fields are represented by red and black contours, respectively. The precipitation fields, which are represented by blue contours and discussed above, are displayed together with convergence and condensation fields in Figure 7. In Figures 7a and 7b, these fields at 17:00 LST around the initial stage of cloud development are shown in the control run and the low-aerosol run, respectively. Around the northwest corner of the domain, there is the initial formation of the convergence field in both the runs at 17:00 LST. The condensation and precipitation rates are on and around the convergence field in both the runs in Figures 7a and 7b due to above-mentioned fact that the convergence field induces updrafts which produce condensation and thus precipitation.

Atmos. Chem. Phys. Discuss., https://doi.org/10.5194/acp-2018-126
Manuscript under review for journal Atmos. Chem. Phys.
Discussion started: 20 February 2018

Atmospheric Chemistry and Physics
Open Access
Discussions

As seen in the comparisons between Figure 7a (Figure 7b) at 17:00 LST and Figure 7c (Figure 7d) at 19:00 LST for the control run (low-aerosol run), the initial convergence field around the northwest corner of the domain at 17:00 LST extends to the east as time progresses. At 19:00 LST, when it comes to the convergence lines or field in the green rectangle as seen in Figures 7c and 7d, the field in the rectangle in the control run is stronger than that in the low-aerosol run. In the control run, the averaged intensity of the convergence field over an area with non-zero convergence in the green rectangle is 0.009 s^{-1} at 19:00 LST. In the low-aerosol run, the averaged intensity of the convergence field in the green rectangle is 0.006 s^{-1} at 19:00 LST. The convergence field in the green rectangle is strongest among the convergence lines over the whole domain and, associated with this, stronger updrafts and greater condensation develop in that field in the green rectangle than in the other lines over the whole domain in each of the runs. Thus, most of heavy precipitation (produced by the stronger updrafts) occurs in the field (surrounded by the green rectangle) in each of the runs (Figure 7).

As seen in the comparisons between Figures 7a and 7c (Figures 7b and 7d) before 20:00 LST and Figure 7e (Figure 7f) at 20:00 LST for the control run (the low-aerosol run), the overall eastward extension of the convergence field over the whole domain continues in both of the runs. In particular, accompanying this extension is the eastward movement of the convergence field in the green rectangle and the associated more intensification of the field in the rectangle, which has the strongest intensity among the convergence lines over the whole domain in each of the runs, in the control run than in the low-aerosol run. Here, the movement of the convergence field and associated heavy precipitation in the green rectangle is tracked down from 19:00 LST on and based on this, the location of the green rectangle is determined in the following hours after 19:00 LST. As in the previous hours, at 20:00 LST, more than 90 % of the heavy precipitation events occurs on and around the convergence field in the green rectangle in the control run (Figures 7c and 7e). At 20:00 LST, in the control run, the averaged intensity of the field over an area with non-zero convergence in the green rectangle is 0.012 s^{-1}, while in the low-aerosol run, the averaged intensity of the field in the green rectangle is 0.007 s^{-1}. The percentage difference in the intensity between the runs increases from 50 % at 19:00 LST to 71 % at 20:00 LST. The fact that most of heavy precipitation is in the green rectangle creates contrast in precipitation rates between the convergence field in the green rectangle and the convergence spots to its west and east, and thus, the high-degree inhomogeneity in the spatial distribution of precipitation rates in the control run (Figures 7c and 7e). Due to the stronger convergence field at 20:00 LST, there is more condensation occurring over the field in the green rectangle in the control run than in the low-aerosol run. The averaged condensation rate over an area with non-zero condensation rate in the green rectangle at 20:00 LST is 1.22 and 0.72 g m^{-3} h^{-1} in the control run and the low-aerosol run, respectively. Associated with this, at 20:00 LST, much more heavy precipitation (with rates above 60 mm hr^{-1}) events occur on and around the convergence field in the green rectangle in the control run than in the low-aerosol run as seen in Figures 7e and 7f. This is the main cause of the greater frequency of heavy precipitation over the whole domain in the control run than in the low-aerosol run when time reaches 20:00 LST as seen in Figure 6c. Also, associated with the stronger convergence field (in the green rectangle), the maximum precipitation rate is higher in the control run (~130 mm hr^{-1}) than in the low-aerosol run (~110 mm hr^{-1}) when time reaches 20:00 LST (Figure 6c).

Even after 20:00 LST, the eastward movement of the convergence field in the green rectangle in the runs and its more intensification in the control run continue. At 23:00 LST, the averaged intensity of the convergence field over an area with non-zero convergence in the green rectangle is ~0.018 s^{-1} in the control run, while in the low-aerosol run, the averaged intensity of the convergence field is ~0.010 s^{-1} (Figures 7g and 7h). The percentage difference in the intensity between the runs increases from 71 % at 20:00 LST to 80 % at 23:00 LST. As in the previous hours, most of the heavy precipitation events occur on and around the convergence field (having the strongest intensity) in the green rectangle in the control run at 23:00 LST as seen in Figure 7g. Due to the stronger convergence field in the green rectangle at 23:00 LST, there is more condensation occurring over the convergence field in the green rectangle in the control run than in the low-aerosol run. The averaged condensation rate over an area with non-zero condensation rate in the green rectangle at 23:00 LST is 1.61 and 0.90 g m^{-3} h^{-1} in the control run and the low-aerosol run, respectively. Associated with this, more heavy precipitation events occur on and around the convergence field in the green rectangle in the control run than in the low-aerosol run at 23:00 LST. When time reaches 23 LST, this

Atmos. Chem. Phys. Discuss., https://doi.org/10.5194/acp-2018-126
Manuscript under review for journal Atmos. Chem. Phys.
Discussion started: 20 February 2018

contributes to the greater frequency of heavy precipitation over the whole domain in the control run than in the low-aerosol run as seen in Figure 6d. Associated with more intensification of the convergence field in the green rectangle after 20:00 LST as compared to the situation before 20:00 LST, the maximum precipitation increases from ~130 to ~180 mm hr^{-1} in the control run as time progresses to 23:00 LST (Figures 6c and 6d). However, associated with less intensification of the convergence field in the green rectangle in the low-aerosol run after 20:00 LST as compared to the situation in the control run, the maximum precipitation in the low-aerosol run does not increase much and increases from ~110 to ~120 mm hr^{-1} with the time progress to 23:00 LST (Figures 6c and 6d).

Figure 4a shows the field of observed aerosol number concentrations at 19:00 LST in the control run. As discussed above, there is the high-degree inhomogeneity in the spatial distribution of aerosol number concentrations. In particular, the area that is surrounded by the red line marks the eastern part of where there is substantial reduction or transition from the high-value aerosol concentration of ~9000 cm^{-3} to the low-value aerosol concentration of ~700 cm^{-3}. It is interesting that most of the strong convergence field (surrounded by the green rectangle) is included in this transition or boundary zone between the high-value and low-value aerosol concentrations (which is surrounded by the red line) at 19:00 LST in the control run (Figures 4a, 7c and 8c). Figure 8c shows the red line in Figure 4a and the green rectangle in Figure 7c for a better observation of the inclusion.

Figure 9a shows the horizontal distribution of wind-vector field (arrows) superimposed upon the field of convergence, condensation, and precipitation at 19:00 LST in the control run. In general, in the area with the high-value aerosol concentration to the west of the strong convergence field (surrounded by the green rectangle), there is the stronger horizontal movement of air than in the area with the low-value aerosol concentration to the east of the strong convergence field. In that area with the high-value aerosol concentration, there is greater cloud-liquid evaporation occurring than in that area with the low-value aerosol concentration in the control run as shown in Figure 10a. Figure 10a shows the vertical distribution of the time- and domain-averaged cloud-liquid evaporation rates over each of the areas to the west and east of the strong convergence field (surrounded by the green rectangle) and over the period between 17:00 and 19:00 LST for the control run and the low-aerosol run. For the calculation of the averaged values in Figure 10, the area to the west (east) of the strong convergence field is set to include all parts of the north-south or the y-direction and the vertical domains but a portion of the east-west or the x-direction domain that extends from the western boundary of Domain 3 to 85 km where the western boundary of the green rectangle is located (from 115 km where the eastern boundary of the green rectangle is located to the eastern boundary of Domain 3) in Domain 3.

The high-value aerosol concentration reduces autoconversion and in turn, increases cloud liquid as a source of evaporation and thus, cloud-liquid evaporation as compared to the low-value aerosol concentration. Also, with the high-value aerosol concentration, there is an increase in the surface-to-volume ratio of cloud droplets and this increases the evaporation efficiency and thus, cloud-liquid evaporation as compared to the situation with the low-value aerosol concentration. Increases in evaporation in turn enhance negative buoyancy, which induces stronger downdrafts in the area with the high-value aerosol concentration than in the area with the low-value aerosol concentration in the control run as seen in Figure 10b. Figure 10b shows the vertical distribution of the time- and domain-averaged downdraft mass fluxes over each of the areas to the west and east of the strong convergence field (surrounded by the green rectangle) for the control run and the low-aerosol run over the period between 17:00 and 19:00 LST. After reaching the near-surface altitudes below ~3 km, in the control run, stronger downdrafts spread out as stronger outflow or horizontal movement as seen in the area with high-value aerosol concentration as compared to those in the area with low-value aerosol concentration in Figure 9a. Then, stronger outflow in the area with high-value aerosol concentration collides with surrounding air or air with weaker horizontal movement in the area with the low-value aerosol concentration. This collision mainly occurs in the places where the transition or boundary between the high-value aerosol concentration and the low-value aerosol concentration is located (surrounded by red line in Figure 4a) as seen in Figures 4a and 9a. This collision creates the strong convergence field, which is surrounded by the green rectangle in those places in the control run as seen in Figures 7c and 9a. The strong convergence field in the green rectangle generates a large amount of condensation and

Atmos. Chem. Phys. Discuss., https://doi.org/10.5194/acp-2018-126
Manuscript under review for journal Atmos. Chem. Phys.
Discussion started: 20 February 2018

Atmospheric Chemistry and Physics Discussions

cloud liquid and this large amount of cloud liquid produces not only heavy precipitation but also high-degree evaporation. Then, the high-degree evaporation in turn contributes to the occurrence of stronger convergence field in the green rectangle, which establishes feedbacks between the convergence field, condensation, and evaporation. This enables the intensification of the green-rectangle convergence field with time while it moves eastward.

Note that, associated with aerosol concentration in the western part of the domain, which is two times greater in the control run than in the low-aerosol run, there is two times greater difference in aerosol concentrations between the area with the high-value aerosol concentration and that with the low-value aerosol concentration in the control run than in the low-aerosol run. This leads to two times greater reduction or transition in aerosol concentrations, particularly in the area surrounded by red line in the control run than in the low-aerosol run (Figure 4). Associated with this, there are greater reduction in autoconversion and increases in cloud liquid and surface-to-volume ratio of cloud droplets in the area with the high-value aerosol concentration in the control run than in the low-aerosol run. Then, there are greater evaporation, the intensity of downdrafts, and associated outflow around the surface in that area in the control run than in the low-aerosol run (Figures 9 and 10). This means that there is stronger collision between outflow and the surrounding air in the control run than in the low-aerosol run, and stronger collision forms the strong convergence field (in the green rectangle) which is much more intense in the control run than in the low-aerosol run as seen in Figure 7. Over this much more intense convergence field, there is the formation of stronger updrafts that are able to form stronger convection, which is in turn able to produce more events of heavy precipitation in the control run than in the low-aerosol run (Figure 6). The more intense strong convergence field in the green rectangle establishes the stronger feedbacks between the convergence field, condensation, and evaporation in the control run than in the low-aerosol run. Hence, the difference in intensity of the green-rectangle convergence field between the runs gets greater as time progresses.

4.3 Sensitivity tests

Atmos. Chem. Phys. Discuss., https://doi.org/10.5194/acp-2018-126
Manuscript under review for journal Atmos. Chem. Phys.
Discussion started: 20 February 2018

4.3.1 Evaporative cooling

It is discussed that cloud-liquid evaporative cooling plays an important role in the formation of the strong convergence field where most of heavy precipitation occurs (surrounded by the green rectangle) in the control run. To confirm this role, we repeat the control run and the low-aerosol run with cooling from cloud-liquid evaporation turned off and cooling from rain evaporation left on. The repeated control run and the low-aerosol run are referred to as the control-noevp run and the low-aerosol-noevp run, respectively. In these repeated runs, cloud-liquid mass reduces due to cloud-liquid evaporation, although cloud-liquid evaporation does not affect temperature.

Due to the absence of cloud-liquid evaporative cooling, there is no formation of the strong convergence field (as seen in the green rectangle in the control run and the low-aerosol run) in these repeated runs as shown in Figures 11a and 11b. Figures 11a and 11b show the convergence field at the surface over the whole domain in the control-noevp run and the low-aerosol-noevp run, respectively, at 23:00 LST which corresponds to the mature stage of the system. Note that the strong convergence field is clearly distinguishable in its intensity and length from any other convergence lines in each of the control run and the low-aerosol run as seen in Figure 7. However, there is no field in each of the repeated runs that is distinguishable in their intensity and length from other lines as seen in Figures 11a and 11b. This leads to the situation where there is no particular convergence field in the control-noevp run that produces much more events of heavy precipitation than those in the low-aerosol-noevp run. This in turn leads to the situation where differences in the frequency of heavy precipitation with rates above 60 mm hr^{-1} between the repeated runs is, on average, only ~10 % of those between the control run and the low-aerosol run, although the control-noevp run shows greater frequency of heavy precipitation than the low-aerosol-noevp run. This is seen in a comparison between the repeated runs, the control run, and the low-aerosol run in Figure 6f that shows the frequency for those runs over the period between 20:00 and 23:00 LST. This comparison demonstrates that cloud-liquid evaporative cooling and its differences between the control run and the low-aerosol run play a key role in much more events of heavy precipitation in the control run than in the low-aerosol run.

4.3.2 Inhomogeneity of aerosol concentration

Remind that between the control run and the low-aerosol run, there are changes not only in the inhomogeneity in the spatial distribution of aerosol concentrations but also in aerosol concentrations. This means that differences between those runs are caused not only by changes in the inhomogeneity but also by those in aerosol concentrations. Although there have been many studies on the effects of changes in aerosol concentrations or loading on heavy precipitation, studies on those effects of changes in the inhomogeneity have been rare. Motivated by this, as a preliminary step to the understanding of those effects of changes in the homogeneity, here, we attempt to isolate the effects of changes in the inhomogeneity on heavy precipitation from those in aerosol concentrations or vice versa. For the isolation, the control run and the low-aerosol run are repeated with homogeneous spatial distributions of background aerosol concentrations. These repeated runs are referred to as the control-homoge run and the low-aerosol-homoge run. The control-homoge run has 2500 cm^{-3} as a concentration of the background aerosol over the whole domain and the whole simulation period. The low-aerosol-homoge run has 1400 cm^{-3} as a concentration of the background aerosol over the whole domain and the whole simulation period. Hence, in the control-homoge run and the low-aerosol-homoge run, the inhomogeneity (or the contrast) in the spatial distribution of aerosol concentrations between the area with the high-value aerosol concentration and that with the low-value aerosol concentration is removed, which achieves the homogeneous spatial distributions. The background aerosol concentration in the control-homoge run (the low-aerosol-homoge run) is the time- and domain-averaged concentration of the background aerosol in the control run (the low-aerosol run).

With the homogeneity in the spatial distribution of aerosol concentrations, there is no formation of the strong convergence field that is distinguishable from any other lines in the control-homoge run and low-aerosol-homoge run as seen in Figures 11c and 11d. Figures 11c and 11d show the convergence field over the whole domain at 23:00 LST in the control-homoge run and the low-aerosol-homoge run, respectively. In the absence of the inhomogeneity between the area with the high-value aerosol concentration and that

Atmos. Chem. Phys. Discuss., https://doi.org/10.5194/acp-2018-126
Manuscript under review for journal Atmos. Chem. Phys.
Discussion started: 20 February 2018

Atmospheric Chemistry and Physics Discussions
Open Access
EGU

with the low-value aerosol concentration, there are no differences in evaporative cooling and outflow between those areas and thus, there is no strong convergence field which is distinguishable from any other lines.

Comparisons between the control run and the control-homoge run (the low-aerosol run and the low-aerosol-homoge run) isolate the effects of the inhomogeneity on heavy precipitation from those of aerosol concentrations whose averaged value is set at 2500 (1400) cm^{-3} for both of the runs. Due to the absence of the inhomogeneity in the spatial distribution of aerosol concentrations, the frequency of heavy precipitation in the control-homoge run and in the low-aerosol-homoge run is, on average, just ~12 and ~10 % of that in the control run and in the low-aerosol run, respectively, over the mature stage (Figure 6g). Hence, the presence of the inhomogeneity alone (in the absence of changes in aerosol concentrations) increases the number of the heavy-precipitation events by a factor of ~ 10. This presence alone also results in a substantial increase in the maximum precipitation rate in the control run and the low-aerosol run as compared to the repeated runs over the mature stage. Between the low-aerosol run and the low-aerosol-homoge run, the increase is from 80 mm hr^{-1} in the low-aerosol-homoge run to 120 mm hr^{-1} in the low-aerosol run, while between the control run and the control-homoge run, the increase is significant and from 90 mm hr^{-1} in the control-homoge run to 180 mm hr^{-1} in the control run (Figure 6g). Here, we see that even without the effects of changes in aerosol concentrations, the presence of the inhomogeneity alone is able to cause the significant enhancement of heavy precipitation in terms of its frequency and maximum value.

Remember that there is an identical domain-averaged background aerosol concentration at each time step between the control run and the control-homoge run and between the low-aerosol run and the low-aerosol-homoge run. Hence, the change in the averaged aerosol concentration between the control-homge run and the low-aerosol-homoge run is identical to that between the control run and the low-aerosol run. With this identical change in the averaged aerosol concentration, between the control run and the low-aerosol run, there is an additional change in the homogeneity. The absence of the strong convergence field in the control-homoge run results in the situation where the increase in the frequency of heavy precipitation in the control-homoge run as compared to that in the low-aerosol-homoge run is, on average, just ~10 % of the increase in the

Atmos. Chem. Phys. Discuss., https://doi.org/10.5194/acp-2018-126
Manuscript under review for journal Atmos. Chem. Phys.
Discussion started: 20 February 2018

Atmospheric Chemistry and Physics Discussions

control run as compared to the low-aerosol run over the mature stage between 20:00 and 23:00 LST (Figure 6g). With the identical change in the averaged aerosol concentration between a pair of the control run and the low-aerosol run and a pair of the control-homoge run and the low-aerosol-homoge run, this demonstrates that the additional change in the inhomogeneity of aerosol distributions plays a much more important role in aerosol-induced increases in the occurrence of heavy precipitation than the change in the averaged aerosol concentrations.

5. Summary and conclusion

This study examines how aerosol affects heavy precipitation or torrential rain in an urban metropolitan area. For this examination, a case that involves a MCS and torrential rain over Seoul, Korea is simulated. This case has the high-degree inhomogeneity of aerosol spatial distributions which involve the high-value aerosol concentration in the western part of the domain and the low-value aerosol concentration in the eastern part of the domain.

It is well-known that increases in aerosol concentrations reduce autoconversion and increase cloud liquid as a source of evaporation, which enhance evaporation and associated cooling. Hence, the high-value aerosol concentration in the western part of the domain causes high-value evaporative cooling rates, while the low-value aerosol concentration in the eastern part of the domain causes low-value evaporative cooling rates. Greater evaporative cooling produces greater negative buoyancy and more intense downdrafts in the western part than in the eastern part. More intense downdrafts then turn into stronger outflow over the western part that collides with surrounding air over the eastern part to form a strong convergence field along the boundary between those parts. Over this strong convergence field, most of heavy precipitation or torrential rain forms. When the contrast in aerosol concentrations between the western and eastern parts or the inhomogeneity of aerosol spatial distributions reduces together with reducing aerosol loading over the western part, the difference in evaporative cooling and outflow between those parts decreases substantially. This results in a much weaker convergence field along the boundary, which is followed by much less occurrences of heavy-precipitation

Atmos. Chem. Phys. Discuss., https://doi.org/10.5194/acp-2018-126
Manuscript under review for journal Atmos. Chem. Phys.
Discussion started: 20 February 2018

events as compared to those with the greater contrast. It is found that the changing inhomogeneity has much more impacts on heavy precipitation than the changing aerosol loading.

Studies (e.g., Niyogi et al., 2006; Thielen et al., 2000) have shown that at the edge of a city, due to a stark contrast in the surface roughness (representing the surface property) between the city and surrounding rural areas, there are enhanced convergence and updrafts. The urban heat island (UHI) effect, which is associated with the surface property in the city, also results in enhanced convergence and updrafts at the edge of the city (Ryu et al., 2013; Schmid and Niyogi, 2017). In addition, a city has stronger and more aerosol sources than surrounding rural areas, hence, the contrast in aerosol concentrations at the edge of a city or at the urban/rural boundary, which is characterized by the contrast in the surface property between the urban and rural areas, is unlikely to be rare. This study suggests that in case there is this type of contrast in aerosol properties such as aerosol concentration at the boundary, there can be enhanced convergence and updrafts at the edge of a city. Hence, this study suggests that the urban/rural contrast in aerosol should be considered as an additional factor (in addition to the contrast in the surface roughness and the UHI effect) to understand the enhancement of convergence and updrafts at the edge of a city.

It should be noted that the urban surface properties, which are represented by the roughness and control the UHI effect, and their contrast with the rural surface properties do not vary significantly with respect to time and space as compared to the variation of aerosol properties. Hence, the location of the urban/rural boundary does not change with time and space significantly. However, in contrast to this, aerosol properties vary substantially with respect to time and space and thus the location of boundary between high-aerosol concentrations and low-aerosol concentrations vary with respect to time and space substantially. For example, in a place within a city away from the city boundary, there can be a sudden increase in traffic and due to the movement of this traffic, the location of this increase can vary spatiotemporally. Then, the boundary between a place with low-aerosol concentrations and the place with the sudden increase in traffic or high-aerosol concentrations can vary spatiotemporally within the city. This indicates that the boundary between the place with high-aerosol concentrations and that with low-aerosol

Atmos. Chem. Phys. Discuss., https://doi.org/10.5194/acp-2018-126
Manuscript under review for journal Atmos. Chem. Phys.
Discussion started: 20 February 2018

concentrations does not necessarily have to be co-located with the urban/rural boundary which is characterized by the contrast in the surface property between the urban and rural areas and whose location does not change much with respect to time and space. Demonstrating this, in this study, the high-aerosol/low-aerosol boundary, which is, for example, surrounded by the red line in Figures 4a and 4b, is not co-located with the urban/rural boundary but located in the middle of the domain or Seoul area. Considering that on the high-aerosol/low-aerosol boundary, heavy precipitation is concentrated in this study, the spatiotemporal variation of the boundary leads to a spatiotemporal variation of heavy precipitation or torrential rain within a city as shown in this study. Hence, while previous theories on urban heavy precipitation can explain heavy precipitation on urban/rural boundary (characterized by the surface-property contrast) and are not able to explain heavy precipitation in various locations within a city, the findings in this study elucidate a mechanism behind heavy precipitation in various locations in a city and thus give us more comprehensive understanding of torrential rain in urban areas.

There are numerous factors that control the spatial distribution of updrafts and associated condensation. Note that changes in this distribution induce those in the spatial distribution of precipitation that may involve the generation of or the enhancement of torrential rain. One of the factors is found to be increasing aerosol concentrations by previous studies (e.g., Khain et al., 2005; Seifert and Beheng, 2006; van den Heever and Contton, 2007; Tao et al., 2007; Storer et al., 2010; Tao et al., 2012; Lee and Feingold, 2013; Lee et al., 2017). These previous studies have found that increasing aerosol concentrations can alter the vertical and horizontal gradient of latent heating and cooling by altering the spatial distributions of freezing, evaporation, and condensation. This alteration leads to that in updrafts, cloud cells, and precipitation, which involves the generation or the enhancement of torrential rain. However, these studies have focused only on increasing aerosol concentrations and assumed that background aerosol concentrations are spatially distributed in a homogeneous fashion or not considered the effect of the inhomogeneity of aerosol spatial distribution on the spatial distribution of latent-heat processes, cloud dynamics, and precipitation. For example, the previous studies have found that aerosol-induced localized changes in evaporation for individual cloud cells can create subsequent localized changes in the horizontal gradient of latent cooling and temperature in and around individual cloud cells. Note that each of these individual localized changes is limited to each of individual localized areas in and around each of individual cloud cells. These changes lead to the generation or the enhancement of torrential rain in and around individual cloud cells. It is found that the increasing inhomogeneity of aerosol concentrations also changes or increases the gradient of evaporation and temperature. These changes lead to the increases in the occurrence of heavy precipitation in a specific area which is along the high-aerosol/low-aerosol boundary and is not limited to a localized area in and around a cloud cell. It is demonstrated that the increasing inhomogeneity plays a much more important role in aerosol-induced increases in the occurrence of heavy precipitation than the increases in aerosol concentrations with their homogeneous spatial distributions.

Acknowledgements

This study is supported by the United States National Oceanic and Atmospheric Administration (Grant NOAA-NWS-NWSPO-2015-2004117), and the National Strategic Project-Fine particle of the National Research Foundation of Korea (NRF) funded by the Ministry of Science and ICT (MSIT), the Ministry of Environment (ME), and the Ministry of Health and Welfare(MOHW) (NRF-2017M3D8A1092022). This study is also supported by the GEMS program of the Ministry of Environment, Korea and the Eco Innovation Program of KEITI (2012000160003).

Atmos. Chem. Phys. Discuss., https://doi.org/10.5194/acp-2018-126
Manuscript under review for journal Atmos. Chem. Phys.
Discussion started: 20 February 2018

Atmospheric Chemistry and Physics Discussions

References

Bouvette T, Lambert JL, and Bedient PB (1982) Revised rainfall frequency analysis for Houston. J Hydraul Div Proc Amer Soc Civil Eng 108: 515–528.

Brown A, Milton S, Cullen M, Golding B, Mitchell J, and Shelly A (2012) Unified modeling and prediction of weather and climate: A 25-year journey. Bull Am Meteorol Soc 93: 1865–1877.

Burian SJ, and Shepherd JM (2005) Effects of urbanization on the diurnal rainfall pattern in Houston: Hydrological processes. Rainfall Hydrol Proc 19: 1089–1103.

Chen F, and Dudhia J (2001) Coupling an advanced land-surface hydrology model with the Penn State-NCAR MM5 modeling system. Part I: Model description and implementation. Mon Wea Rev 129: 569–585.

Chen S., et al. (2015) Urbanization effect on precipitation over the Pearl River Delta based on CMORPH data. Adv Clim Chang Res 6: 16-22.

Dhar, ON, and Nandergi, S (1993) The zones of severe rainstorm activity over India. Int J Climatol13: 301-311.

Diem JE, and Brown DP (2003) Anthropogenic impacts on summer precipitation in central Arizona. USA Prof Geogr 55: 343–355.

Fan J,, Yuan, T., Comstock, , J. M., et al. (2009) Dominant role by vertical wind shear in regulating aerosol effects on deep convective clouds. J Geophys Res114: doi:10.1029/2009JD012352.

Fouquart Y, and Bonnel B (1980) Computation of solar heating of the Earth's atmosphere: a new parameterization. Beitr Phys Atmos 53: 35-62.

Fujibe F (2003) Long-term surface wind changes in the Tokyo metropolitan area in the afternoon of sunny days in the warm season. J Meteor Soc Japan 81: 141–149.

Holben BN, Tanré D, Smirnov A, Eck TF, Slutsker I, Abuhassan N, Newcomb W W, Schafer JS, Chatenet B, Lavenu F, Kaufman YJ, Castle JV, Setzer A, Markham B, Clark D, Frouin R, Halthore R, Karneli A, O'Neill NT, Pietras C, Pinker RT, Voss K, and Zibordi G (2001) An emerging ground-based aerosol climatology: Aerosol optical depth from AERONET. J Geophys Res 106: 12067–12097.

Hwang S-O, and Lee D-K (1993) A study on the relationship between heavy rainfalls and

Atmos. Chem. Phys. Discuss., https://doi.org/10.5194/acp-2018-126
Manuscript under review for journal Atmos. Chem. Phys.
Discussion started: 20 February 2018

Atmospheric Chemistry and Physics Discussions

associated low-level jets in the Korean peninsula. J. Korean Meteorol. Soc. 29: 133–146.

Khain A. (2009) Notes on state-of-the-art investigations of aerosol effects on precipitation: a critical review. Environ Res Lett 4: doi:10.1088/1748-9326/4/1/015004.

Khain A, BenMoshe N, and Pokrovsky A (2008) Factors determining the impact of aerosols on surface precipitation from clouds: Attempt of classification. J Atmos Sci 65: 1721-1748.

Khain A, Rosenfeld D, and Pokrovsky A (2005) Aerosol impact on the dynamics and microphysics of deep convective clouds. Quart J Roy Meteor Soc 131: 2639-266..

Korea Meteorological Administration (2011) Heavy rainfall events top 10, KMA registered Pub., No. 11-136000-000833-01, Seoul, Korea, 48 p.

Lebo ZJ, and Morrison H (2014) Dynamical effects of aerosol perturbations on simulated idealized squall lines. Mon Wea Rev 142: 991-1009.

Lee D-K, Kim H-R, and Hong S-Y (1998) Heavy rainfall over Korea during 1980–1990. Korean J Atmos Sci 1: 32–50.

Lee SS, Donner LJ, Phillips VTJ, and Ming Y (2008a) Examination of aerosol effects on precipitation in deep convective clouds during the 1997 ARM summer experiment. Q J R Meteorol Soc 134: 1201-1220.

Lee SS, Donner LJ, Phillips VTJ, and Ming Y (2008b) The dependence of aerosol effects on clouds and precipitation on cloud-system organization, shear and stability. J Geophys Res 113: D16202.

Lee SS, and Feingold G (2013) Aerosol effects on the cloud-field properties of tropical convective clouds. Atmos Chem Phys 13: 6713-6726.

Lee SS, Li Z, Mok J, et al. (2017) Interactions between aerosol absorption, thermodynamics, dynamics, and microphysics and their impacts on clouds and precipitation in a multiple-cloud system. Clim Dyn: https://doi.org/10.1007/s00382-017-3552-x, 2017.

Lee SS, Kim B-G, and Yum SS, et al. (2016) Effect of aerosol on evaporation, freezing and precipitation in a multiple cloud system. Clim Dyn 48: 1069-1087.

Li Z, Niu F, Fan J, Liu Y, Rosenfeld D, and Ding Y (2011) Long-term impacts of

Atmos. Chem. Phys. Discuss., https://doi.org/10.5194/acp-2018-126
Manuscript under review for journal Atmos. Chem. Phys.
Discussion started: 20 February 2018

Atmospheric Chemistry and Physics Discussions

aerosols on the vertical development of clouds and precipitation. Nat Geosci 4: 888-894.

Mannan Md A, Chowdhury Md A, and Karmakar S (2013) Application of NWP model in prediction of heavy rainfall in Bangladesh, Pac. Sci. 56: 667-675.

Mladek, et al. (2000) Intercomparison and evaluation of precipitation forecasts for MAP seasons 1995 and 1996. Meteorol Atmos Phys 72: 111-129.

Mlawer EJ, Taubman SJ, Brown PD, Iacono MJ, and Clough SA (1997) RRTM, a validated correlated-k model for the longwave. J Geophys Res 102: 16663-1668.

Morrison H, and Grabowski WW (2011) Cloud-system resolving model simulations of aerosol indirect effects on tropical deep convection and its thermodynamic environment. Atmos Chem Phys 11: 10503–10523.

Niyogi D, Holt T, Zhong S, Pyle PC, and Basara J (2006) Urban and land surface effects on the 30 July 2003 mesoscale convective system event observed in the southern Great Plains. J Geophys Res 111: 1–20.

Ryu Y-H, Baik J-J, and Han J-Y (2013) Daytime urban breeze circulation and its interaction with convective cells. Q J R Meteorol Soc 139: 401–413.

Sauer VB, Thomas WO, Stricker VA, and Wilson KV (1984) Flood characteristics of urban watersheds in the United States, United States Geological Survey Water-Supply Paper 2207, pp 63.

Schmid PE, and Niyogi D (2017) Modeling urban precipitation modification by spatially heterogeneous aerosols. J Appl Meteorol Climatol: https://doi.org/10.1175/JAMC-D-16-0320.1.

Seifert A, and Beheng KD (2006) A two-moment cloud microphysics parameterization for mixed-phase clouds. Part 2: Maritime vs. continental deep convective storms. Meteorol Atmos Phys 92: 67-82.

Shepherd, JM (2005) A review of current investigations of urban-induced rainfall and recommendations for the future. Earth Interact 9: 1-27.

Storer RL, van den Heever SC, and Stephens GL (2010) Modeling aerosol impacts on convection under differing storm environments. J Atmos Sci 67: 3904-3915. Sun J, and Lee T-Y (2002) A numerical study of an intense quasistationary convection band over the Korean peninsula. J Meteorol Soc Jpn 80: 1221–1245.

Atmos. Chem. Phys. Discuss., https://doi.org/10.5194/acp-2018-126
Manuscript under review for journal Atmos. Chem. Phys.
Discussion started: 20 February 2018

Sun J,, and Lee T-Y (2002) A numerical study of an intense quasistationary convection band over the Korean peninsula. J Meteorol Soc Jpn 80:1221–1245.

Takahashi H (2003) Secular variation in the occurrence property of summertime daily rainfall amount in and around the Tokyo metropolitan area (in Japanese with an English abstract). Tenki 50: 31–41.

Tao W-K, Chen J-P, Li Z., Wang C, and Zhang C (2012) Impact of aerosols on convective clouds and precipitation. Rev Geophys 50: RG2001.

Tao W-K, Li X, Khain A, Matsui T, Lang S, and Simpson J (2007) Role of atmospheric aerosol concentration on deep convective precipitation: Cloud-resolving model simulations. J Geophys Res 112: D24S18.

Thielen J, Wobrock W, Gadian A, Mestayer P, and Creutin J-D (2000) The possible influence of urban surfaces on rainfall development: a sensitivity study in 2D in the meso-γ-scale, Atmos Res 54: 15–39.

United Nations (2015) Department of Economic and Social Affairs, Population Division: World urbanization prospects: The 2014 Revision, (ST/ESA/SER.A/366), https://esa.un.org/unpd/wup.

van den Heever SC., and Cotton WR (2007) Urban aerosol impacts on downwind convective storms. J Appl Meteorol Clim 46: 828–850.

Wang H, Skamarock WC, and Feingold G (2009) Evaluation of scalar advection schemes in the Advanced Research WRF model using large-eddy simulations of aerosol-cloud interactions. Mon Wea Rev 137: 2547-2558.

Wang Y, Zhang R, Saravanan R (2014) Asian pollution climatically modulates mid-latitude cyclones following hierarchical modelling and observational analysis. Nature Comm 5: 3098.

Yeh H-C, and Chen GT-J (2004) Case study of an unusually heavy rain event over eastern Taiwan during the Mei-Yu Season. Mon Wea Rev 132: 320-337.

Atmos. Chem. Phys. Discuss., https://doi.org/10.5194/acp-2018-126
Manuscript under review for journal Atmos. Chem. Phys.
Discussion started: 20 February 2018

FIGURE CAPTIONS

Figure 1. Triple-nested domains used in the CSRM simulations. The boundary of the figure itself is that of Domain 1, while the rectangles marked by "d02" and "d03" represent the boundary of Domain 2 and Domain 3, respectively.

Figure 2. 850 hPa wind (m s^{-1}; arrows), geopotential height (m; contours), and equivalent potential temperature (K; shaded) at 21:00 LST July 26^{th} 2011 over Northeast Asia. The rectangle in the Korean Peninsula in the panel marks Domain 3.

Figure 3. Aerosol size distribution at the surface. N represents the aerosol number concentration per unit volume of air and D represents the aerosol diameter.

Figure 4. Spatial distributions of background aerosol number concentrations at the surface (black contours; in "$\times\ 10^3$ cm^{-3}") and the boundary of each area that has precipitation rate of 60 mm hr^{-1} or above (blue contours) in Domain 3 at (a) 19:00 LST and (b) 20:00 LST. Red lines in panels (a) and (b) mark a part of the domain where there is a substantial reduction in aerosol number concentrations (see text for the details of red lines). Panels (c) and (d) are the same as panels (a) and (b), respectively, but with the reduced contrast in aerosol number concentrations for the low-aerosol run (see text for the details of the reduced contrast).

Figure 5. Area-mean precipitation rate at the surface smoothed over 3 hours for the control run, the low-aerosol run, and observation in Domain 3.

Figure 6. Frequency distribution of the precipitation rates at the surface, which are collected over the whole domain, for (a) the whole simulation period, (b) a period between 17:00 and 19:00 LST, (c) a period between 19:00 and 20:00 LST, (d) a period between 20:00 and 23:00 LST, and (e) a period between 04:00 and 05:00 LST in the control run and the low-aerosol run. In panel (a), observed frequency which is interpolated to the simulation time steps and grid points is also shown. Panels (f) and (g) are the same as the panel (d) but the control-noevp run and the low-aerosol-noevp run are

Atmos. Chem. Phys. Discuss., https://doi.org/10.5194/acp-2018-126
Manuscript under review for journal Atmos. Chem. Phys.
Discussion started: 20 February 2018

additionally displayed in Panel (f), while the control-homoge run and the low-aerosol-homoge run are additionally displayed in Panel (g).

Figure 7. Spatial distributions of precipitation rates at the surface (blue contours), convergence at the surface (red contours), and the column-averaged condensation rates (black contours). Green rectangles in Panels (c), (d), (e), (f), (g), and (h) mark areas with heavy precipitation and are described in detail in text. Panels (a), (c), (e) and (g) are for the control run, while panels (b), (d), (f) and (h) are for the low-aerosol run. Panels (a) and (b) are for 17:00 LST, and panels (c) and (d) are for 19:00 LST, while panels (e) and (f) are for 20:00 LST, and panels (g) and (h) are for 23:00 LST. In panels (a) and (b), red contours are at 0.4 and 0.7 × 10^{-2} s^{-1} and black contours are at 0.4 and 0.9 g m^{-3} h^{-1}. In panels (a) and (b), blue contours are at 10.0 and 30.0 mm h^{-1}. In panels (c) and (d), red contours are at 0.9 and 1.7 × 10^{-2} s^{-1}, black contours are at 0.9 and 1.5 g m^{-3} h^{-1}, and blue contours are at 10.0, 30.0, and 50.0 mm h^{-1}. In panels (e) and (f), red contours are at 1.4 and 2.3 × 10^{-2} s^{-1} and black contours are at 1.3 and 2.9 g m^{-3} h^{-1}. In panels (e) and (f), blue contours are at 10.0, 50.0, 100.0, and 130.0 mm h^{-1}. In panels (g) and (h), red contours are at 2.1 and 3.5 × 10^{-2} s^{-1} and black contours are at 2.3 and 3.8 g m^{-3} h^{-1}. In panels (g) and (h), blue contours are at 10.0, 30.0, 60.0, and 130.0 mm h^{-1}.

Figure 8. Boundary of each area which has the observed surface precipitation rate of 60 mm hr^{-1} or above (blue contours) and a specific area (surrounded by the green rectangle and described in text related to Figure 7) where heavy precipitation is concentrated in the runs in Domain 3 at (a) 19:00 LST and (b) 20:00 LST. Panel (c) shows the red line which marks the eastern part of where there is a substantial reduction or transition from the high-value aerosol concentration of ~9000 cm^{-3} to the low-value aerosol concentration of ~700 cm^{-3}, as described in text related to Figure 4a, and the green rectangle at 19:00 LST.

Figure 9. Panels (a) and (b) are the same as Figures 7c and 7d, respectively, but with wind-vector fields (arrows) that are superimposed on the fields in Figures 7c and 7d.

Figure 10. Vertical distributions of the time- and domain-averaged (a) cloud-liquid evaporation rates and (b) downdraft mass fluxes over each of the areas to the west and east of the strong convergence field for the control run and the low-aerosol run over a period between 17:00 and 19:00 LST (see text for details).

Figure 11. Spatial distributions of convergence at the surface at 23:00 LST. Panels (a), (b), (c), and (d) are for the control-noevp run, the low-aerosol-noevp run, the control-homoge run, and the low-aerosol-homoge run, respectively, and contours are at 2.1 and 3.5×10^{-2} s^{-1}.

Atmos. Chem. Phys. Discuss., https://doi.org/10.5194/acp-2018-126
Manuscript under review for journal Atmos. Chem. Phys.
Discussion started: 20 February 2018

Simulations	Contrast in aerosol spatial distribution	The effect of Cloud-liquid evaporation on temperature	The homogeneous aerosol distribution
Control run	Observed	Present	Absent
Low-aerosol run	Reduced by a factor of 2	Present	Absent
Control-noevp run	Observed	Absent	Absent
Low-aerosol-noevp run	Reduced by a factor of 2	Absent	Absent
Control-homoge run	Observed	Present	Present
Low-aerosol-homoge run	Reduced by a factor of 2	Present	Present

Table 1. Summary of simulations

Atmos. Chem. Phys. Discuss., https://doi.org/10.5194/acp-2018-126
Manuscript under review for journal Atmos. Chem. Phys.
Discussion started: 20 February 2018

Atmospheric Chemistry and Physics Discussions
Open Access

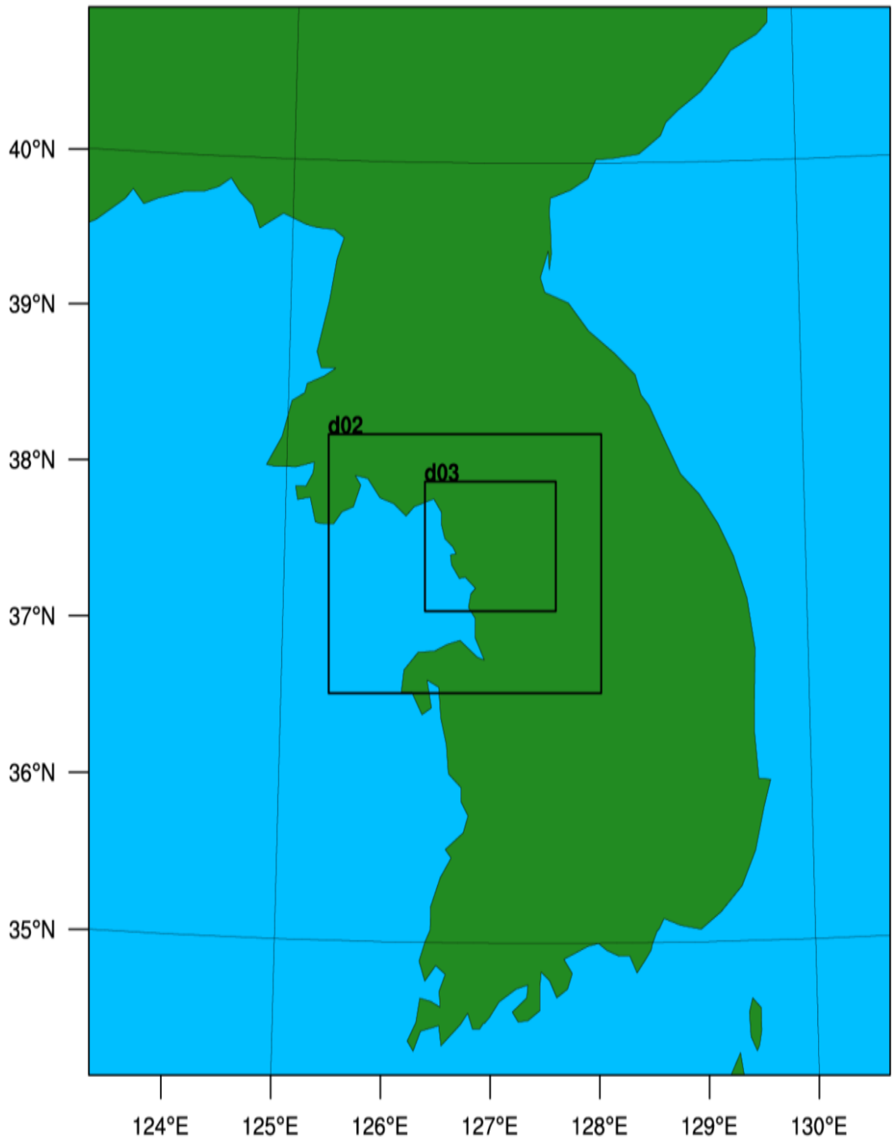

1058

1059 **Figure 1**

Atmos. Chem. Phys. Discuss., https://doi.org/10.5194/acp-2018-126
Manuscript under review for journal Atmos. Chem. Phys.
Discussion started: 20 February 2018

Atmospheric Chemistry and Physics
Open Access
Discussions

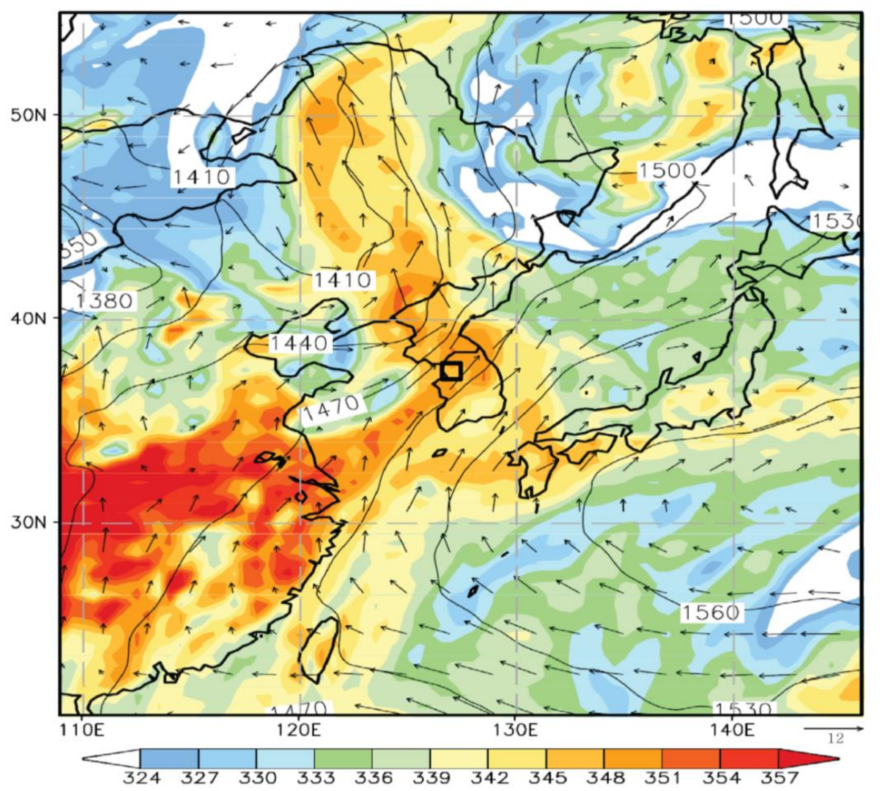

Figure 2

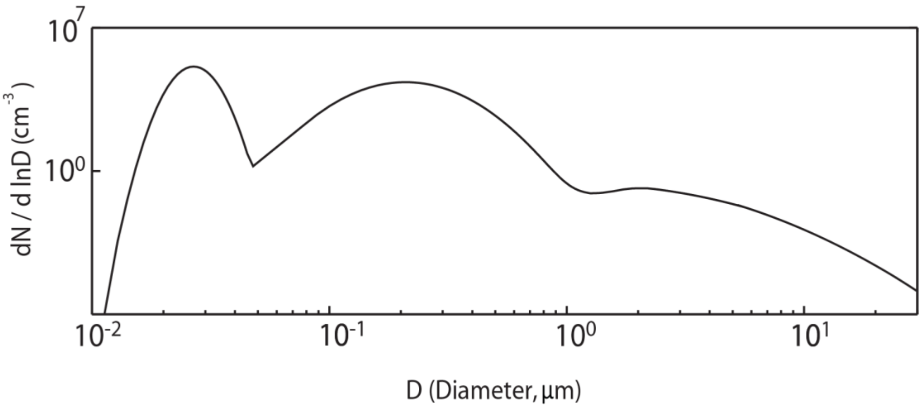

Figure 3

Atmos. Chem. Phys. Discuss., https://doi.org/10.5194/acp-2018-126
Manuscript under review for journal Atmos. Chem. Phys.
Discussion started: 20 February 2018

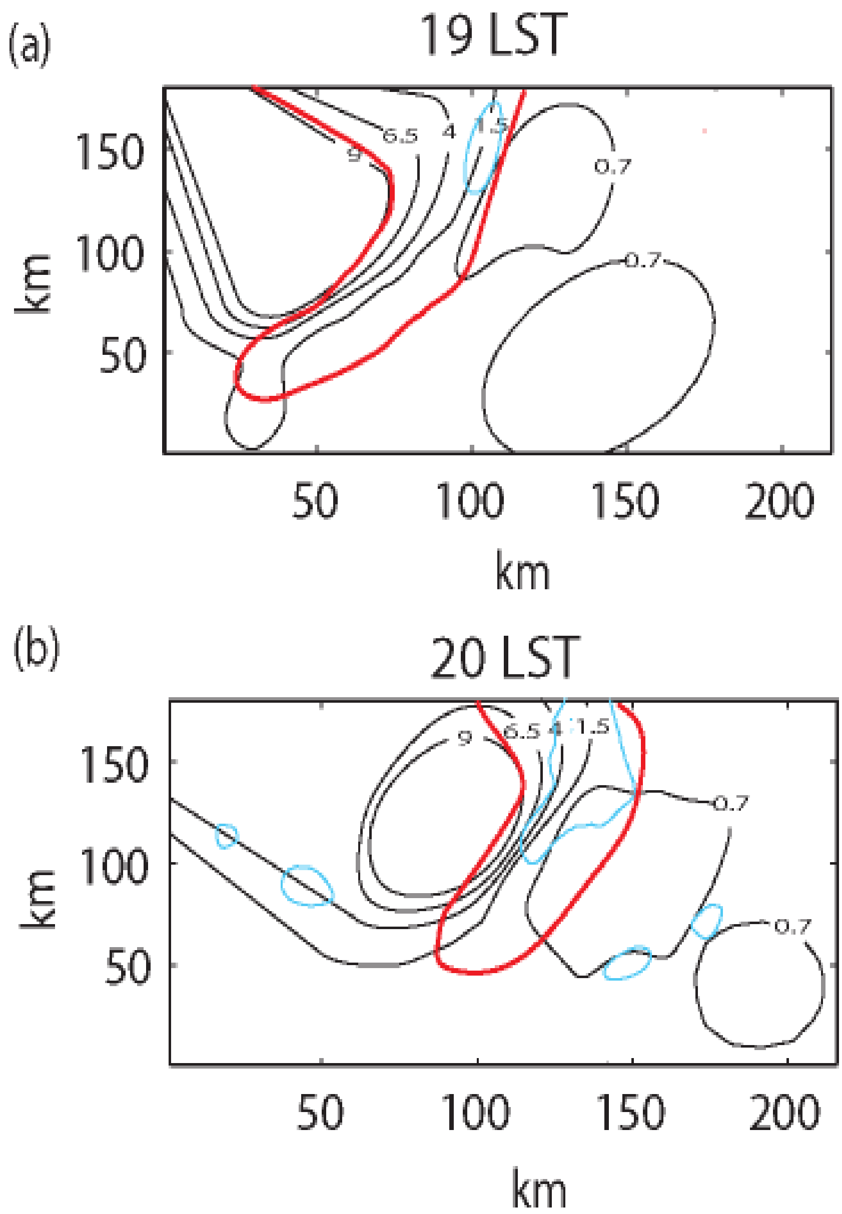

1068

1069 **Figure 4**

1070

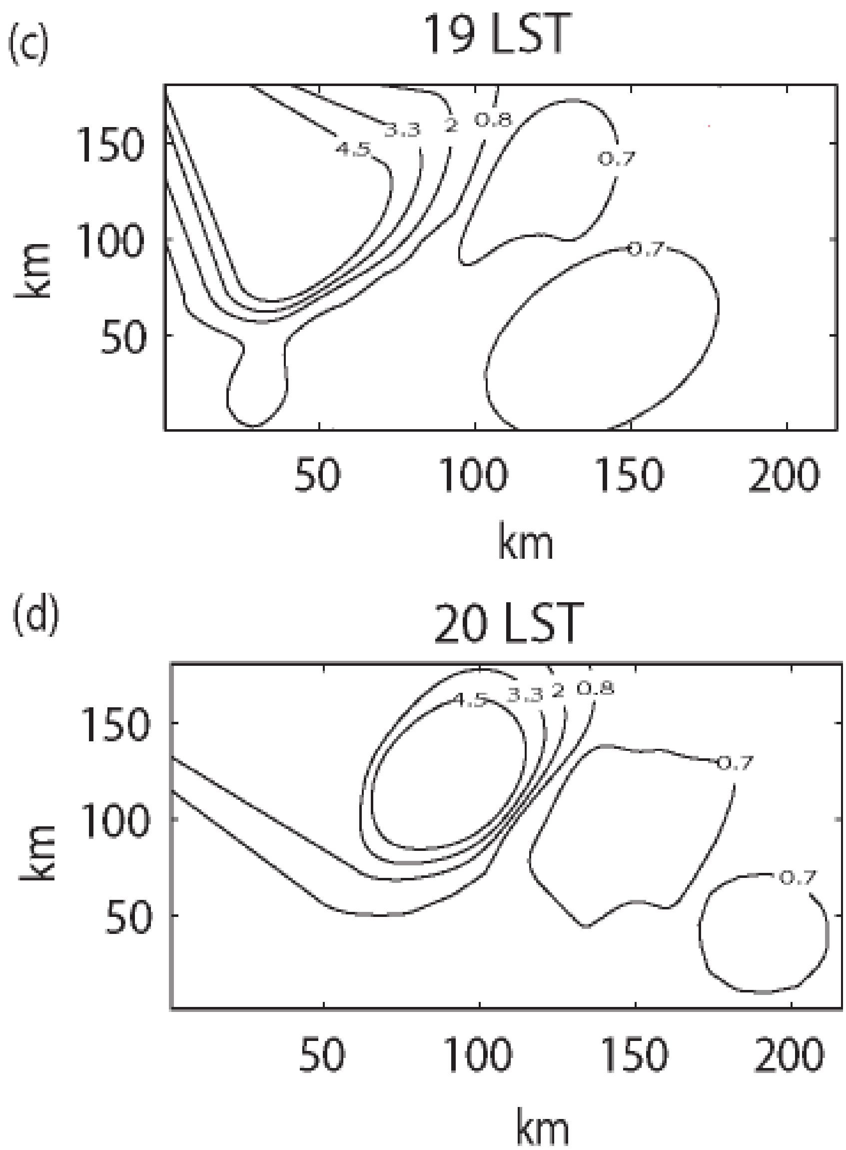

1071

1072 **Figure 4**

1073

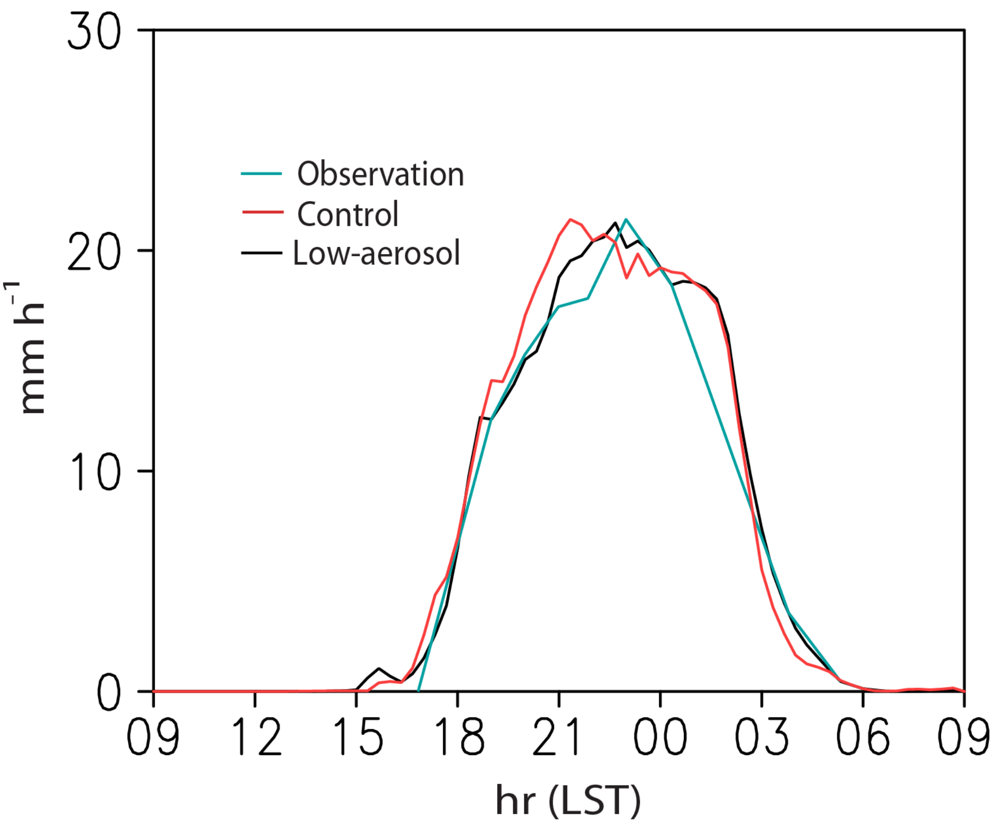

1074

1075 **Figure 5**

1076

1077

1078

1079

1080

1081

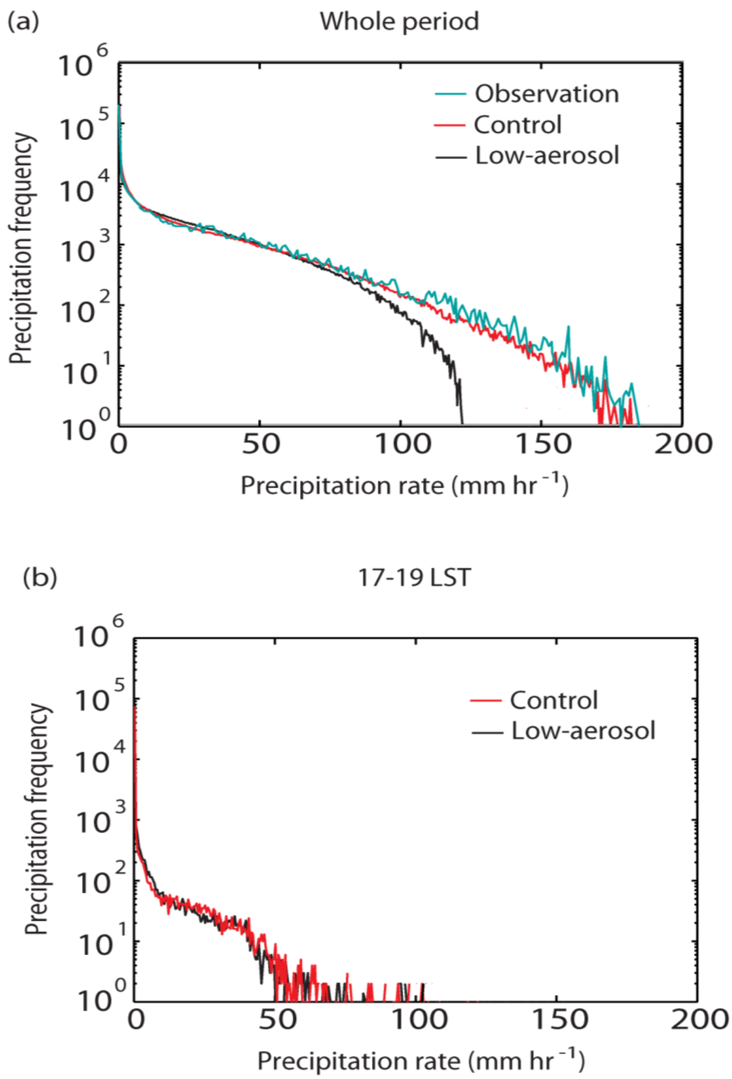

1082

1083 **Figure 6**

1084

1085

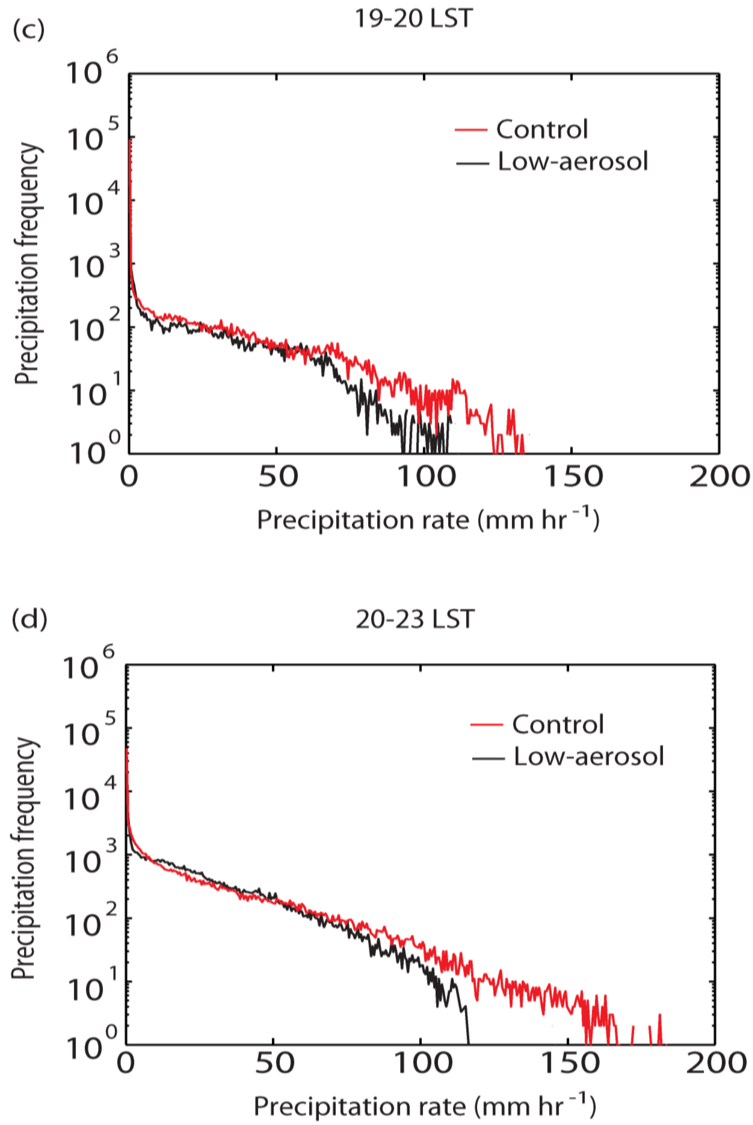

1086

1087 **Figure 6**

1088

1089

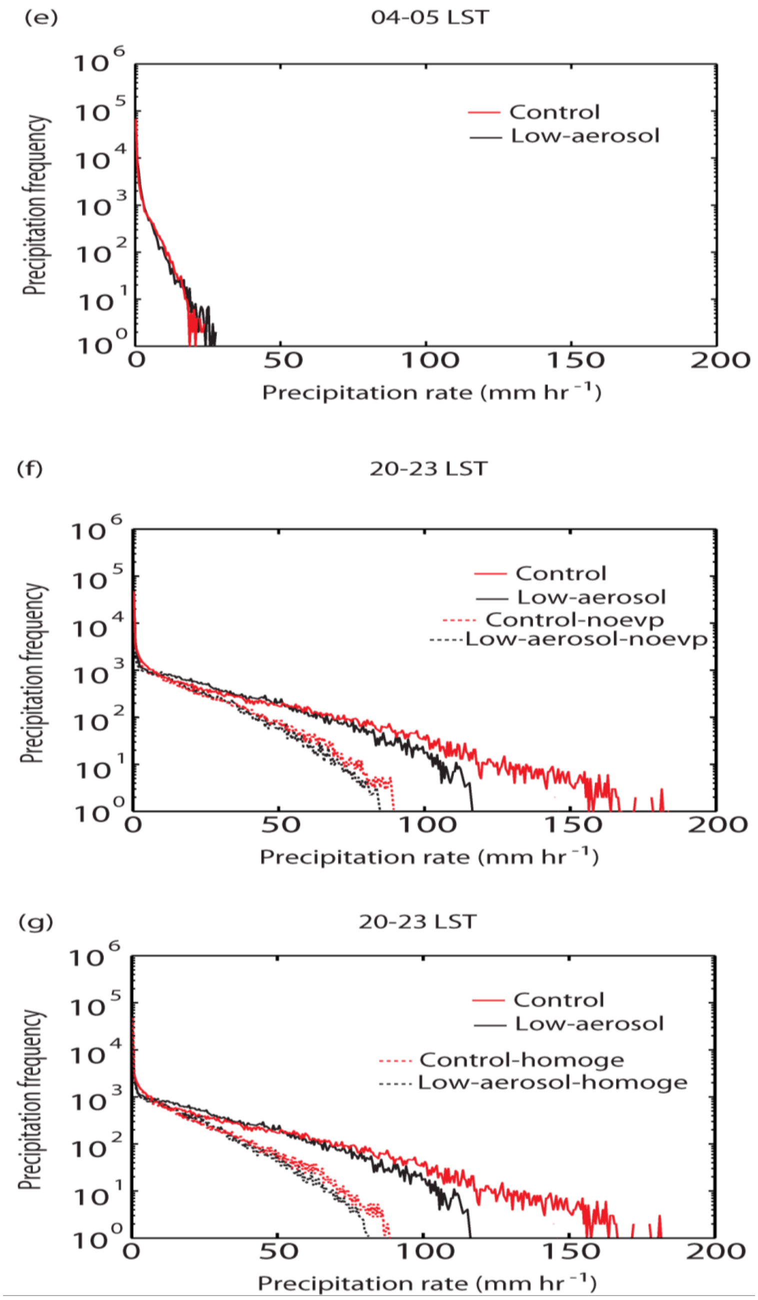
(e)
04-05 LST
Control
Low-aerosol
Precipitation frequency
Precipitation rate (mm hr⁻¹)
(f)
20-23 LST
Control
Low-aerosol
Control-noevp
Low-aerosol-noevp
Precipitation frequency
Precipitation rate (mm hr⁻¹)
(g)
20-23 LST
Control
Low-aerosol
Control-homoge
Low-aerosol-homoge
Precipitation frequency
Precipitation rate (mm hr⁻¹)

Figure 6

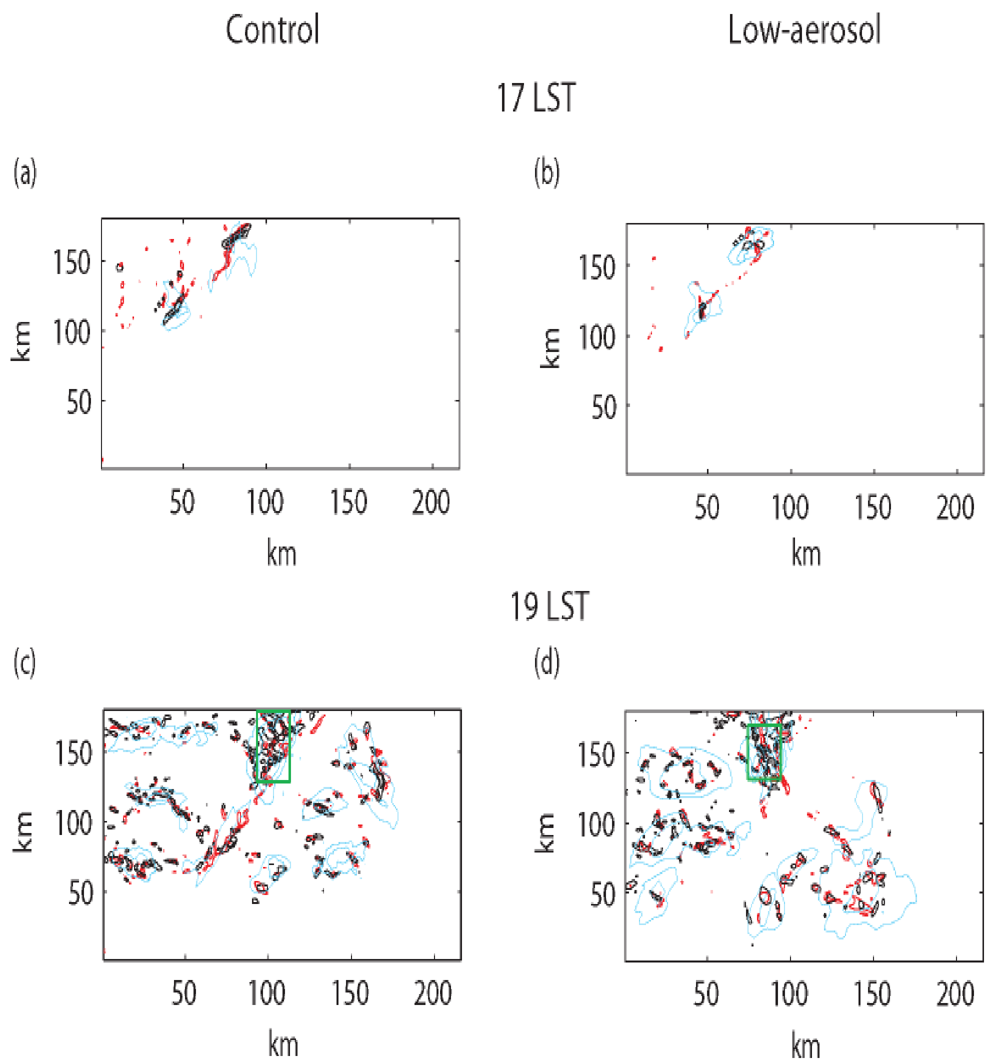

1092

1093 **Figure 7**

1094

1095

1096

1097

1098

1099

1100

1101

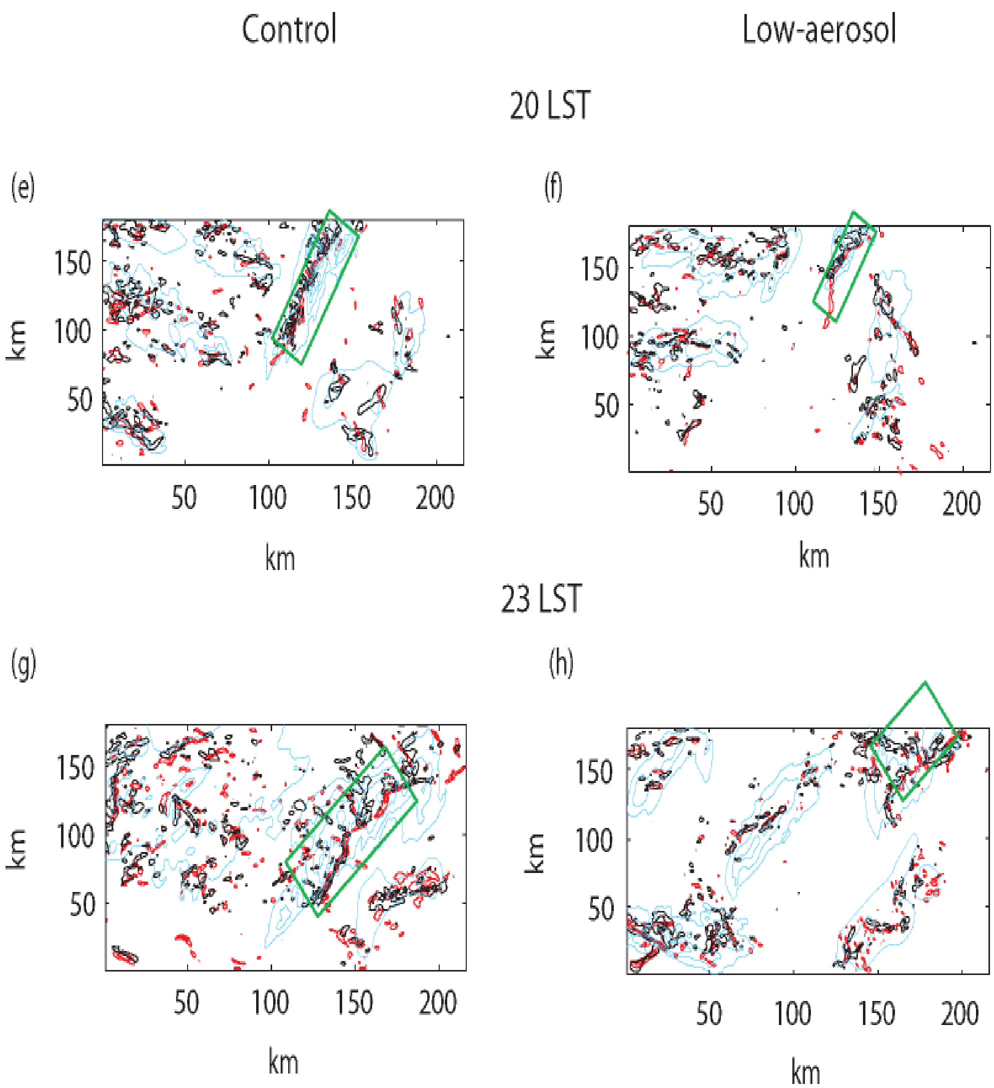

1102
1103
1104 **Figure 7**
1105
1106
1107
1108

Atmos. Chem. Phys. Discuss., https://doi.org/10.5194/acp-2018-126
Manuscript under review for journal Atmos. Chem. Phys.
Discussion started: 20 February 2018

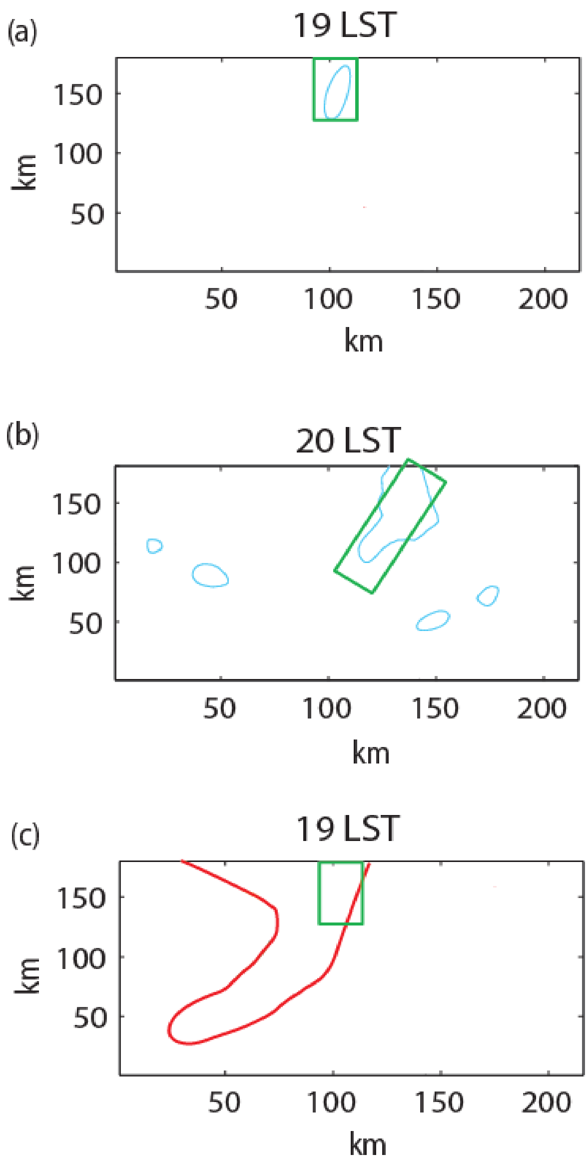

Figure 8

Atmos. Chem. Phys. Discuss., https://doi.org/10.5194/acp-2018-126
Manuscript under review for journal Atmos. Chem. Phys.
Discussion started: 20 February 2018

Atmospheric Chemistry and Physics Discussions
Open Access

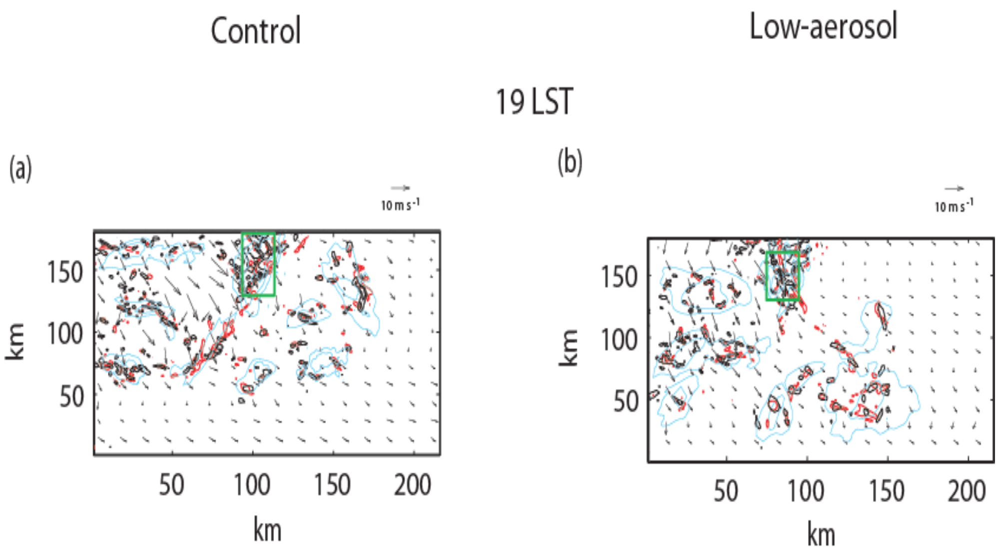

Figure 9

Atmos. Chem. Phys. Discuss., https://doi.org/10.5194/acp-2018-126
Manuscript under review for journal Atmos. Chem. Phys.
Discussion started: 20 February 2018

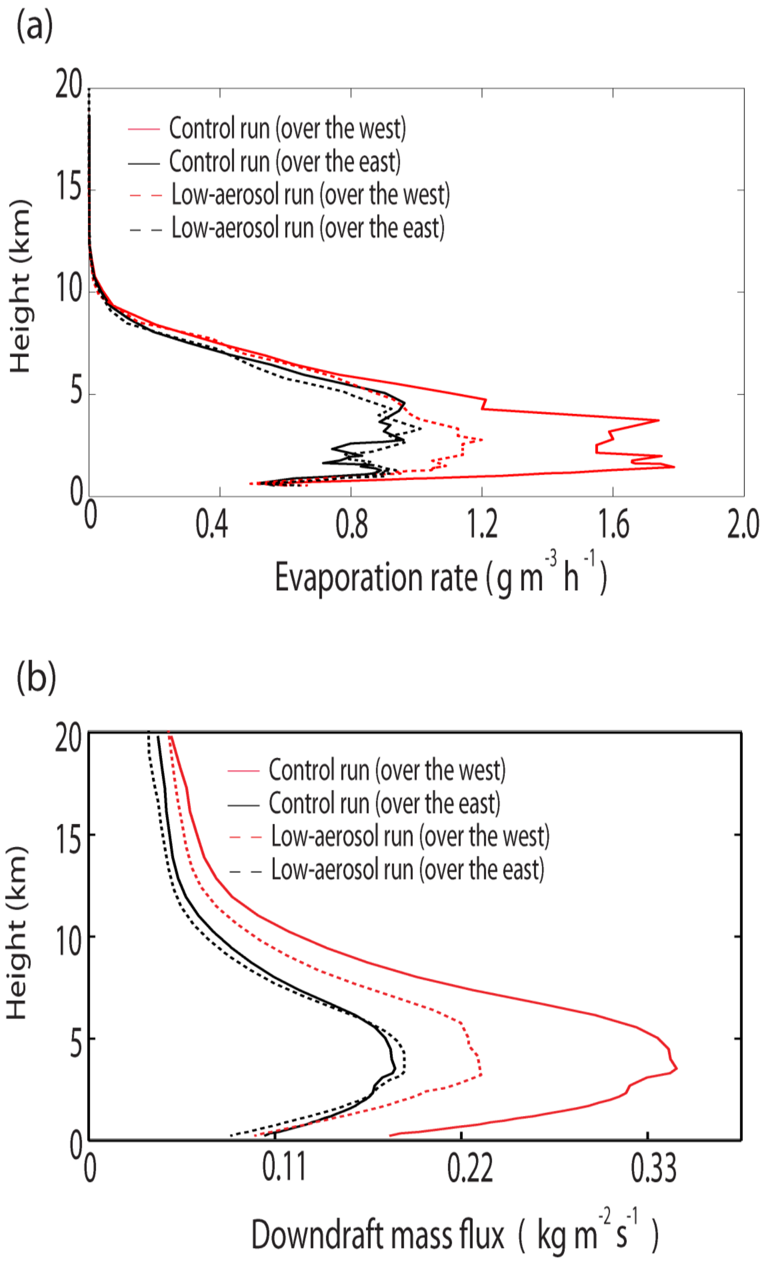

1122

1123 **Figure 10**

1124

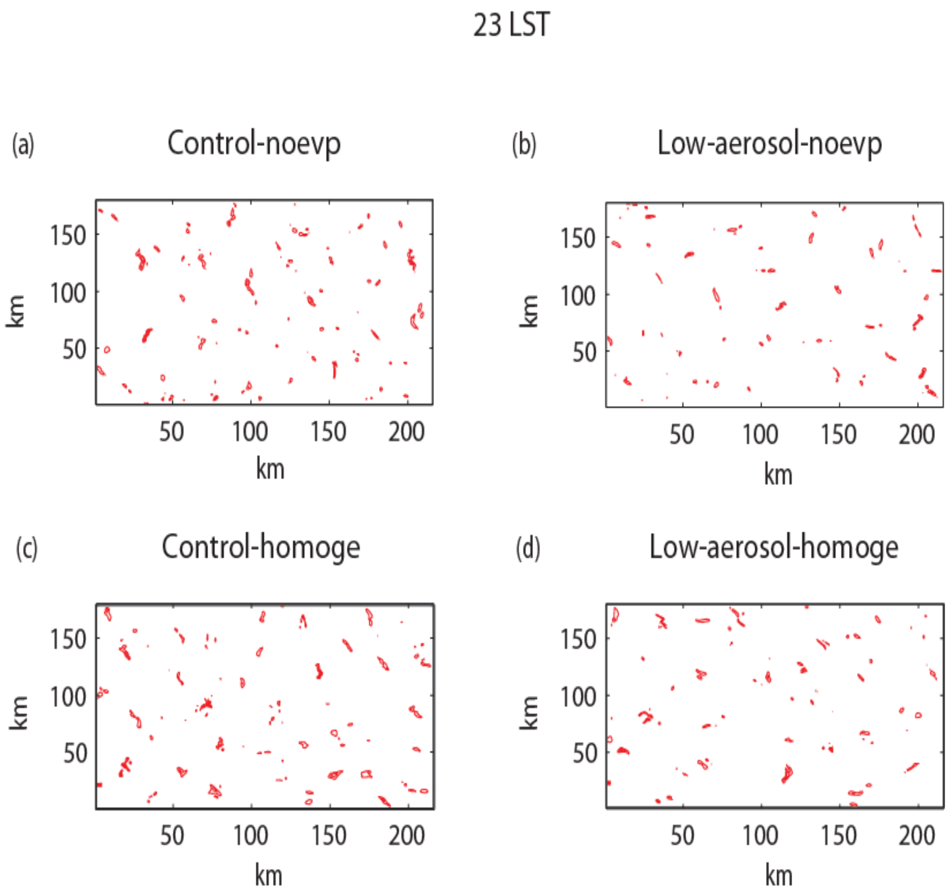
23 LST
(a)
Control-noevp
(b)
Low-aerosol-noevp
(c)
Control-homoge
(d)
Low-aerosol-homoge
km
150
100
50
50
100
150
200
km

Figure 11